Impact of the Depth-to-Width Ratio of Periodically Stratified Tidal Channels on the Estuarine Circulation

ELISABETH SCHULZ

Leibniz Institute for Baltic Sea Research Warnemünde, Rostock, Germany

HENK M. SCHUTTELAARS

Delft Institute of Applied Mathematics, Delft University of Technology, Delft, Netherlands

ULF GRÄWE AND HANS BURCHARD

Leibniz Institute for Baltic Sea Research Warnemünde, Rostock, Germany

(Manuscript received 25 April 2014, in final form 18 May 2015)

ABSTRACT

The dependency of the estuarine circulation on the depth-to-width ratio of a periodically, weakly stratified tidal estuary is systematically investigated here for the first time. Currents, salinity, and other properties are simulated by means of the General Estuarine Transport Model (GETM) in cross-sectional slice mode, applying a symmetric Gaussian-shaped depth profile. The width is varied over four orders of magnitude. The individual along-channel circulation contributions from tidal straining, gravitation, advection, etc., are calculated and the impact of the depth-to-width ratio on their intensity is presented and elucidated. It is found that the estuarine circulation exhibits a distinct maximum in medium-wide channels (intermediate depth-to-width ratio depending on various parameters), which is caused by a maximum of the tidal straining contribution. This maximum is related to a strong tidal asymmetry of eddy viscosity and shear created by secondary strain-induced periodic stratification (2SIPS): in medium channels, transverse circulation generated by lateral density gradients due to laterally differential longitudinal advection induces stable stratification at the end of the flood phase, which is further increased during ebb by longitudinal straining (SIPS). Thus, eddy viscosity is low and shear is strong in the entire ebb phase. During flood, SIPS decreases the stratification so that eddy viscosity is high and shear is weak. The circulation resulting from this viscosity–shear correlation, the tidal straining circulation, is oriented like the classical, gravitational circulation, with riverine outflow at the surface and oceanic inflow close to the bottom. In medium channels, it is about 5 times as strong as in wide (quasi one-dimensional) channels, in which 2SIPS is negligible.

1. Introduction

a. Estuarine circulation

The circulation in tidal estuaries has been investigated for more than half a century, but the driving mechanisms are still not fully understood. In the beginning, only the gravitational (also called gravity-, density-, or buoyancy-driven) circulation was considered (e.g., Pritchard 1952; Agnew 1960; Hansen and Rattray 1965): The salinity (and thus density) decrease from the ocean toward the riverine freshwater reach induces an up-estuary baroclinic pressure gradient force that increases from surface to bottom. The down-estuary barotropic pressure gradient force is vertically constant. Combined, these forces drive an up-estuary bottom flow of saline water and a down-estuary surface flow of fresher water. This is the classical estuarine circulation.

Linden and Simpson (1988) and Simpson et al. (1990) discovered the stratifying and destratifying effect of the vertically sheared ebb and flood current in the presence of a longitudinal (along-channel, axial) salinity gradient: since the absolute velocity increases with the distance from the bottom, the ebb current transports fresher over more saline water, resulting in a stably stratified water

---

Corresponding author address: Elisabeth Schulz, Leibniz Institute for Baltic Sea Research Warnemünde, Seestrasse 15, 18119 Rostock, Germany.
E-mail: e.schulz.fischer@gmail.com

DOI: 10.1175/JPO-D-14-0084.1

column, and the flood current reduces or completely erases this stratification. Simpson et al. (1990) called this process strain-induced periodic stratification (SIPS) and described its dependency on the horizontal gradient Richardson number, now called the Simpson number (Burchard et al. 2011).

Even though it was already known that stratification suppresses turbulence (Linden 1979, 1980) and understood how turbulent mixing reduces the intensity of a density-driven flow (Linden and Simpson 1986), it took some time before the feedback of SIPS on the tidal currents was recognized. Jay and Musiak (1994, 1996) explained how stratification during ebb decreases the eddy viscosity and thus allows stronger shear, that is, surface-enhanced ebb currents, and how a homogeneous water column during flood increases the eddy viscosity and thus prohibits strong flood shear, that is, leads to bottom-enhanced flood currents. The residual (tidally averaged, subtidal) circulation contribution resulting from this tidal asymmetry of eddy viscosity and shear has the same orientation as the classical estuarine circulation and is called tidal straining circulation (Burchard et al. 2011; Geyer and MacCready 2014).

One- and two-dimensional model studies (Burchard and Hetland 2010; Burchard et al. 2011) revealed that this is the dominant circulation contribution in periodically stratified estuaries. The first field observations of tidal straining circulation in tidally energetic, weakly stratified channels (Becherer et al. 2011) supported these results. Current measurements (Stacey et al. 2001) and simulations (Burchard et al. 2011) also showed that the tidal straining circulation can reverse, that is, oppose the orientation of the classical estuarine circulation, when stratification is strong during flood (by lateral straining, see below).

A classical longitudinal salinity gradient provided (salinity decreasing in the up-estuary direction), down-estuary shear and stratification enforce each other (see above, SIPS and tidal straining circulation) until the flow becomes unstable, that is, the instantaneous local gradient Richardson number, Ri $= N^2/S^2$, falls below the critical value of 0.25 [$N^2 = -g/\rho_0\ \partial\rho/\partial z$ Brunt–Väisälä or buoyancy frequency, $S^2 = (\partial u/\partial z)^2 + (\partial v/\partial z)^2$ shear squared; Kundu and Cohen 2002].

The existence of transverse (cross-sectional, secondary) circulation was first postulated by Smith (1976) and confirmed by observations of surface convergence during flood (e.g., Nunes and Simpson 1985). It was attributed to bathymetry-induced lateral (across-channel) shear of the longitudinal tidal current (faster above deep channel), leading to lateral salinity gradients that generate a transverse gravitational circulation. Lerczak and Geyer (2004) described the effect of differential advection of along-channel density gradients and the resulting transverse circulation on the longitudinal momentum and circulation. To clearly indicate the mechanism driving these circulations, we refer to it as laterally differential longitudinal advection (of salinity).

During flood, the salinity increases from the shoals to the thalweg (deepest channel) so that the transverse circulation is surface-convergent. This is called flood-oriented transverse circulation (Burchard et al. 2011). It advects high longitudinal momentum from the surface center downward and low momentum from the shoals toward the thalweg, at the surface, which leads to bottom-enhanced flood currents. During ebb, the salinity decreases from the shoals to the thalweg so that the transverse circulation is surface-divergent. This is called ebb-oriented transverse circulation. It advects high momentum from the surface center toward the shoals and low momentum from the shoals toward the thalweg, at the bottom, which leads to surface-enhanced ebb currents. The residual longitudinal circulation contribution resulting from this tidally asymmetric shear also has the same orientation as the classical estuarine circulation and is called advectively driven circulation (Burchard et al. 2011).

Measurements (e.g., Stacey et al. 2001; Lacy et al. 2003; Becherer et al. 2011; Scully and Geyer 2012; Becherer et al. 2015; Purkiani et al. 2015) and numerical studies (Scully et al. 2009; Purkiani et al. 2015) revealed that transverse circulation can also induce stratification and that this lateral straining process is more important during stronger mixing conditions (flood, spring tide). Thus, stratification can be stronger during flood than during ebb, which is contrary to the longitudinal straining (SIPS, see above).

Field observations and model results (Valle-Levinson et al. 2000; Valle-Levinson 2008; Huijts et al. 2011) showed that transverse circulation and lateral convergence can also result from Coriolis deflection of the longitudinal tidal currents, that is, transverse circulation does not require (but may be enhanced by) salinity gradients. Yet another lateral effect is related to turbulent mixing being constantly high above the shoals and periodic above the channel (Scully and Friedrichs 2007). This gradient increases the phase lag between shoals and channel, particularly around slack after ebb, and drives a laterally sheared residual longitudinal circulation with up-estuary flow above the shoals and down-estuary flow above the channel.

Further possible contributions to the estuarine circulation arise from channel convergence (e.g., Ianniello 1979; Burchard et al. 2014), curvature (Geyer 1993; Chant 2002; Becherer et al. 2015), wind (Scully et al. 2005; Waterhouse et al. 2013), and trapping due to

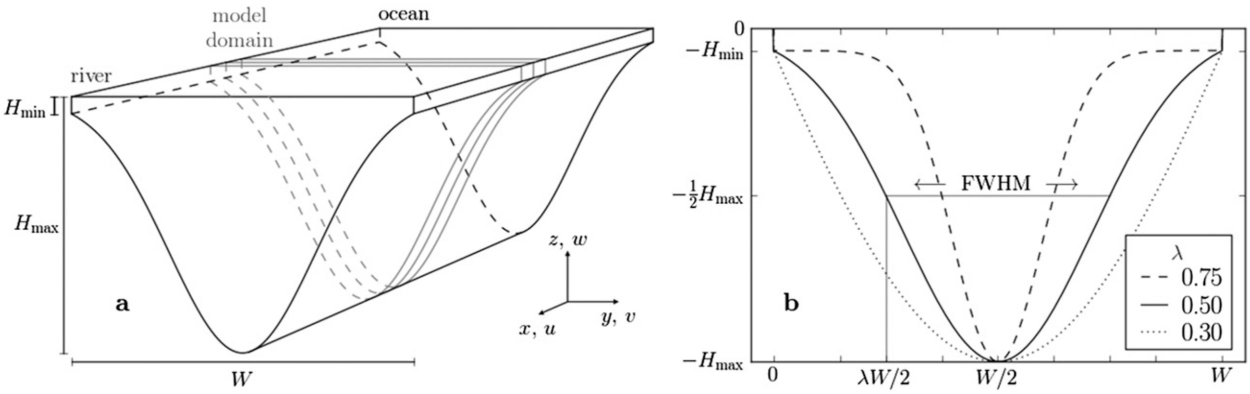

FIG. 1. (a) Schematic of the model domain and its orientation; (b) Gaussian depth profiles for different λ [(9)].

complex geometry (Lacy et al. 2003; Giddings et al. 2012). The reviews by MacCready and Geyer (2010) and Geyer and MacCready (2014) contain comprehensive summaries of estuarine circulation processes.

b. *Motivation*

Lerczak and Geyer (2004) suggested that lateral effects would be stronger in narrower estuaries and recommended further studies to investigate the interaction of the transverse and the longitudinal circulation and the salinity field. Simulations with three different widths (Burchard et al. 2011) could not strongly confirm this assumption but revealed a clear dependency of the tidal straining circulation (and thus the total, estuarine circulation) on the width, with the intensity increasing with the width.

The numerical study presented here provides the first systematic investigation of the impact of the aspect ratio (depth-to-width ratio) on the estuarine circulation. It spans four orders of magnitude of the aspect ratio and shows that the dependency described by Burchard et al. (2011) holds only for narrow and medium-wide estuaries [aspect ratio $\gtrsim$0.004, depending on other parameters; see section 4a(1)]. It reveals that for wider estuaries, the intensity of the dominant, tidal straining circulation decreases with the width, that is, the estuarine circulation is maximum for a certain aspect ratio, a phenomenon we explain here.

Lerczak and Geyer (2004) described how the transverse circulation advects the salinity, together with the longitudinal momentum, and numerous observations revealed its stratifying effect (lateral straining, see above). While the feedback of the momentum advection on the estuarine circulation was recognized (advectively driven circulation), the feedback of the stratification, via the interaction with eddy viscosity and shear (tidal straining circulation), was not considered.

Our study shows that lateral straining ($\partial_z v \partial_y S$) can lead to stratification during or at the end of flood, depending on the aspect ratio. This also has far-reaching consequences for the stratification during ebb, the tidal asymmetry, and the estuarine circulation. We suggest calling this process secondary strain-induced periodic stratification (2SIPS).

This paper is structured as follows. The next section introduces the theoretical background, the channel geometry, and nondimensional numbers. Section 3 explains the two-dimensional numerical model, the parameters, and the analysis of the model output. Then the results are presented and discussed: section 4a describes the impact of the aspect ratio on the estuarine circulation, particularly the tidal straining contribution, and on the eddy viscosity and the stratification; section 4b clarifies the role of lateral and vertical straining and advection for the stratification; and section 4c substantiates the results by means of additional experiments and simulations. In the conclusion, the 2SIPS process and its influence on the longitudinal tidal straining circulation in dependency on the aspect ratio are summarized. The appendixes provide further equations and details of the numerical experiments as well as information on a three-dimensional model.

2. Theory

a. *Basic equations*

We assume an infinitely long, longitudinally uniform, straight, irrotational estuary (Fig. 1a) and use the hydrostatic dynamic equations and the salinity budget equation as given in Burchard et al. (2011) (also see appendix A). The longitudinal barotropic pressure gradient is calculated in such a way that the cross-sectionally averaged longitudinal velocity $\overline{\overline{u}}(t)$ equals a prescribed M_2 tidal current:

$$\overline{\overline{u}}(t) = \frac{1}{A}\int_A u(y,z,t)\,d\hat{A} = U_t \sin(\omega t)\,, \tag{1}$$

where A is the cross-sectional area, U_t is the prescribed cross-sectionally averaged M_2 velocity amplitude, $\omega = 2\pi/T$ is the circular frequency, and $T = 44\,714$ s is the periodic time of the M_2 tidal current.

Note that river discharge is ignored here. Looking into tidal inlet systems such as those in the Wadden Sea, discharge is typically negligible. A horizontal density gradient can also be established with zero discharge, for example, by differential heating (Burchard et al. 2008).

The lateral barotropic pressure gradient is calculated in such a way that the surface elevation is constant, $\eta(y, t) = 0$ (rigid lid). It should be noted that this does not mean that the lateral barotropic pressure gradient is zero, but that it balances the vertically averaged baroclinic pressure gradient so that the vertically integrated lateral velocity vanishes, $\int_{-H(y)}^{0} v(y, z, t)\,dz = 0$ (see Burchard et al. 2011).

The results and sensitivities to parameters obtained with the simplified two-dimensional model (more details in section 3a) are in qualitative agreement with those obtained with a three-dimensional model (appendix B).

We use a simplified equation of state (MacCready and Geyer 2010; Geyer and MacCready 2014):

$$\rho = \rho_0(1 + \beta S)\,, \tag{2}$$

where $\rho(y, z, t)$ is the density, $\rho_0 = 1025\,\mathrm{kg\,m^{-3}}$ is the reference density, $\beta = 7.8 \times 10^{-4}\,\mathrm{psu^{-1}}$ is the haline contractivity, and $S(y, z, t)$ is the salinity. Thus, the buoyancy

$$b = -g(\rho - \rho_0)/\rho_0\,, \tag{3}$$

where g is the gravitational acceleration, becomes

$$b = -g\beta S\,. \tag{4}$$

b. Channel geometry

For the depth profile we choose a Gaussian curve (Fig. 1),

$$H(y) = c_1 + c_2 \exp[-c_3(y - W/2)^2]\,, \tag{5}$$

with W representing the prescribed channel width. The coefficients c_1, c_2, and c_3 are determined by the following conditions:

$$\begin{aligned} H(0) = H(W) &= H_{\min} < H_{\max}/2, \\ H(W/2) &= H_{\max}, \\ H(\lambda W/2) &= H_{\max}/2, \end{aligned} \tag{6}$$

where $H_{\min}$ and $H_{\max}$ are the prescribed minimum and maximum depth at the shores ($y = 0$, W) and the thalweg ($y = W/2$), respectively. The parameter λ is related to the prescribed full width at half maximum depth (FWHM; Fig. 1b):

$$W = \lambda W + \mathrm{FWHM}\,, \tag{7}$$

where λ equals the fraction of the channel width with $H(y) \le H_{\max}/2$ and thus determines the steepness of the channel slopes, together with $H_{\min}$ and the aspect ratio [(11)].

c. Nondimensional numbers

The system described above is characterized by the nine dimensional parameters numbered in Table 1. These parameters involve two dimensions (length in meters and time in seconds) so that the system is well defined by seven linearly independent nondimensional numbers ($9 - 2 = 7$; e.g., Buckingham 1914; Kalagnanam et al. 1994). A possible, and in parts commonly used, set is that given in Table 1.

The Simpson number is also known as the horizontal Richardson number; the unsteadiness number is also known as the Stokes number (Souza 2013) or inverse Strouhal number (Burchard et al. 2011, and references therein). Their dynamic impact and that of the nondimensional bottom roughness length were systematically investigated in previous studies (Burchard and Hetland 2010; Burchard et al. 2011). These studies used the average water depth as length scale, $H = H_{\mathrm{mean}}$, but here we choose the maximum water depth, $H = H_{\max}$, which is independent of the channel shape.

Preliminary tests for the study presented here showed a dependency on the nondimensional quasi-lateral diffusivities of momentum and salinity, $\tilde{A}_{y*} = \tilde{K}_{y*}$, which we define by scaling with the channel width W and the root-mean-square (RMS) friction velocity scale U_*:

$$\tilde{A}_{y*} = A_{y*}/(WU_*)\,. \tag{8}$$

It should be noted that the estuarine circulation decreases with increasing $\tilde{A}_{y*}$. This hints at the importance of lateral processes but is not investigated further.

The remaining three nondimensional numbers describe the channel shape (also see section 2b and Fig. 1b):

$$\lambda = 1 - \mathrm{FWHM}/W\,, \tag{9}$$

$$\tilde{H}_{\min} = H_{\min}/H_{\max}\,, \quad \text{and} \tag{10}$$

$$\alpha = H_{\max}/W\,. \tag{11}$$

TABLE 1. Dimensional parameters and nondimensional numbers with their reference values or variation ranges. The numerals in the first column indicate the system-characterizing nine parameters and seven linearly independent nondimensional numbers. The circles mark model input. The stars mark varied parameters and numbers; others are invariant. Parameters and numbers without an equation are directly prescribed; others are calculated. Sigma is the bottom-following coordinate, $\sigma(y, z) = z/H(y)$; $\kappa = 0.4$ is the von Kármán constant. Note that the quasi-lateral diffusivity of salinity here equals that of momentum, $K_{y*} = A_{y*}$ and $\tilde{K}_{y*} = \tilde{A}_{y*}$.

			Dimensional parameters		Values/ranges
1	∘	★	W	Width (surface)	100–10^6 m
2	∘	★	$\mathrm{FWHM} = (1-\lambda)W$	Full width at half maximum depth	50–0.5×10^6 m
3	∘		$H_{\max}$	Maximum water depth (thalweg)	15 m
4	∘		$H_{\min}$	Minimum water depth (shoals)	1 m
			$H_{\mathrm{mean}} = 1/W \int_0^W H(y)\,dy$	Average water depth	7.8 m
5	∘		z_0^b	Bottom roughness length	0.001 m
	∘		T	M_2 tidal period	44 714 s
6			$\omega = 2\pi/T$	M_2 tidal frequency	$1.4 \times 10^{-4}\,\mathrm{s}^{-1}$
	∘		$\partial_x S$	Longitudinal salinity gradient	$-3 \times 10^{-4}\,\mathrm{psu\,m}^{-1}$
7			$\partial_x b = -g\beta\partial_x S$	Longitudinal buoyancy gradient	$2.3 \times 10^{-6}\,\mathrm{s}^{-2}$
	∘		U_t	Cross-sectionally averaged M_2 velocity amplitude	$1\,\mathrm{m\,s}^{-1}$
8			$U_* = U_t\sqrt{C_D/2}$	RMS friction velocity scale	$0.033\,\mathrm{m\,s}^{-1}$
9	∘	★	$A_{y*} = \tilde{A}_{y*} W U_*$	Quasi-lateral eddy diffusivity along σ layers	0.069–693 $\mathrm{m}^2\,\mathrm{s}^{-1}$
			Nondimensional numbers		Values/ranges
1			$\mathrm{Si} = H_{\max}^2 \partial_x b/U_*^2$	Simpson number	0.48
2			$\mathrm{Un} = H_{\max}\omega/U_*$	Unsteadiness number	0.064
3			$\tilde{z}_0^b = z_0^b/H_{\max}$	Nondimensional bottom roughness length	6.7×10^{-5}
4			$\tilde{A}_{y*}$	Nondimensional quasi-lateral eddy diffusivity	0.021
5			λ	Fraction of W with $H(y) \le H_{\max}/2$	0.5
6			$\tilde{H}_{\min} = H_{\min}/H_{\max}$	Minimum-to-maximum depth ratio	0.067
7		★	$\alpha = H_{\max}/W$	Aspect ratio, depth-to-width ratio	1.5×10^{-5}–0.15
			$C_D = \kappa^2/[(1 + \tilde{z}_0^b)\ln(1 + 1/\tilde{z}_0^b) - 1]^2$	Drag coefficient	2.2×10^{-3}

The focus of our study is on the impact of the aspect ratio α on the estuarine circulation and its contributions.

3. Methods

a. Numerical model, experiments, and setup

The dimensional equations are solved numerically by means of the three-dimensional General Estuarine Transport Model (GETM; http://www.getm.eu) incorporating a two-equation k–ε turbulence closure model [General Ocean Turbulence Model (GOTM; http://www.gotm.net)]. See Burchard et al. (2011) for details on the two-dimensional mode of GETM, that is, the y–z slice model with vanishing longitudinal gradients except for the baroclinic and the barotropic pressure gradients.

To investigate the importance of transverse advection of momentum and salinity for the longitudinal circulation, we carry out further experiments with reduced physics, in addition to the reference experiment [experiment A (full physics); equations in appendix A]: experiment C (no momentum advection), experiment D (no lateral internal pressure gradient), and experiment F (no transverse salinity advection). Experiments C and D have already been carried out by Burchard and Schuttelaars (2012); experiment F is new. [It should be noted that we do not call it B or E in order to avoid confusion with Burchard and Schuttelaars (2012).]

The domain of the cross-sectional slice model is shown in Fig. 1a. It lies in the y–z plane and has a lateral resolution of 200 cells and a vertical resolution of 100 sigma layers with zooming toward the bottom. The surface elevation is constant, $\eta(y, t) = 0$ (rigid lid; see Burchard et al. 2011).

The model is forced by a constant baroclinic pressure gradient and a periodic barotropic pressure gradient [(1)]. The computational time step is $\Delta t = T/20\,000 \approx 2.2\,\mathrm{s}$ except for very narrow channels, for which numerical stability requires $\Delta t = T/40\,000 \approx 1.1\,\mathrm{s}$ ($W \le 300\,\mathrm{m}$) or even $\Delta t = T/80\,000 \approx 0.6\,\mathrm{s}$ ($W \le 100\,\mathrm{m}$). The model is started from rest at slack after ebb and run for 10 tidal cycles to ensure periodicity.

It should be noted that we tested the periodicity as well as the influence of the starting point. If started at slack after flood, the model gives the same results, except for an expectable offset in salinity and thus density and buoyancy.

b. Prescribed parameters

The invariant parameters are prescribed with the reference values listed in Table 1 unless otherwise

TABLE 2. Aspect ratios of several real estuaries, calculated from depth and width as found in the given literature and divided into three size classes [see section 4a(1), Fig. 2]. It should be noted that $H = H_{\mathrm{mean}}$ in the first three examples.

	Estuary	α	H (m)	W (km)	Reference
Wide	Delaware, estuary mouth	1.5×10^{-4}	6.1	40	van Rijn (2011)
	Hooghly, estuary mouth	3.2×10^{-4}	7	22	van Rijn (2011)
	Western Scheldt, estuary mouth	4.0×10^{-4}	10	25	van Rijn (2011)
Medium	York River, near Clay Bank	3.3×10^{-3}	10	3	Scully and Friedrichs (2007)
	Willapa Bay, Stanley Channel	6.7×10^{-3}	20	3	Banas and Hickey (2005)
	Marsdiep Inlet	6.8×10^{-3}	27	4	Buijsman and Ridderinkhof (2008)
	Hudson River, 6 km south of George Washington Bridge	1.3×10^{-2}	15	1.2	Peters (1997)
Narrow	Schillbalje (tidal gat southwest of Wadden Sea island Spiekeroog)	1.5×10^{-2}	15	1	Becherer et al. (2015)
	Fraser River	1.5×10^{-2}	12	0.8	Geyer and Smith (1987)
	Lister Dyb	1.6×10^{-2}	40	2.5	Purkiani et al. (2015)
	San Francisco Bay, Suisun Cutoff	2.4×10^{-2}	12	0.5	Stacey et al. (1999)
	St. Augustine Inlet	2.7×10^{-2}	15	0.55	Waterhouse et al. (2013)
	Ponce de Leon Inlet	3.4×10^{-2}	12	0.35	Waterhouse and Valle-Levinson (2010)
	Conway, Tal-y-Cafn reach	3.9×10^{-2}	5.5	0.14	Nunes and Simpson (1985)

noted. They yield the nondimensional numbers also listed in Table 1, for example, the Simpson number Si = 0.48 and the unsteadiness number Un = 0.064.

For comparison, applying the average water depth and the amplitude of the friction velocity ($U_{*,\mathrm{amp}} = \sqrt{2}U_* = U_t\sqrt{C_D}$) leads to Si = 0.066 and Un = 0.024 and applying the average water depth and the RMS friction velocity leads to Si = 0.13 and Un = 0.034. The latter calculation is in agreement with Burchard et al. (2013) and our values compare well to those given for the York River during spring tide or the Western Scheldt (their Table 1).

In this contribution, we focus on variation of the width with $100\,\mathrm{m} \le W \le 10^6\,\mathrm{m}$, yielding the aspect ratio $0.15 \ge \alpha \ge 1.5 \times 10^{-5}$, that is, spanning four orders of magnitude. This parameter range is investigated with about 60 simulations.

Please note that not the entire α range can be found in reality, but it is used here to also cover marginal phenomena, for example, to show the (transition to) quasi-one-dimensional behavior of wide estuaries. Aspect ratios of several real estuaries are listed in Table 2 for comparison. It should be noted that the model results presented here are not applicable to all of these estuaries since some of them are governed by permanent stratification, Coriolis forcing, or curvature.

To vary α but no other nondimensional number, the full width at half maximum depth and the dimensional quasi-lateral diffusivities ($A_{y*} = K_{y*}$) are varied proportionally to the width so that the channel shape (λ) and the nondimensional diffusivities remain invariant (see Table 1). Instead of varying α by means of W (requiring the variation of FWHM and A_{y*}), α could be varied by means of $H_{\max}$ (requiring the variation of $H_{\min}$, z_0^b, U_t, and A_{y*}), which is slightly more laborious and therefore omitted.

As a side note, if the water depth is varied but z_0^b is not, that is, if the nondimensional bottom roughness length $\tilde{z}_0^b$ is varied (inversely proportionally to α), there is an additional impact on the dynamics. However, this impact is small compared to the impact of α (to be shown): varying $\tilde{z}_0^b$ by two orders of magnitude changes the intensity of the estuarine circulation by only 30% (Burchard et al. 2011, their Table 2).

It should be noted that preliminary tests confirmed self-similarity when the dimensional parameters are varied but the nondimensional numbers are invariant. For example, if $H_{\max}$ is doubled, invariance of the nondimensional numbers requires doubling of $H_{\min}$, z_0^b, W, FWHM, and U_t, as well as quadrupling of A_{y*} and K_{y*}. If this is taken into account, the results of the two simulations are the same.

Please also note that, for the default parameter values (Table 1), Coriolis force has no significant effect on the residual circulation [section 4c(2)].

c. *Analysis and notation*

Velocities (u, v, w), vertical eddy viscosity A_z, and salinity S are analyzed based on the last (tenth) tidal cycle of the model output, when a periodic state is reached. The time and spatial coordinates are nondimensionalized by their characteristic scales:

$$\tilde{t} = t/T, \quad \tilde{y} = y/W, \quad \tilde{z} = z/H_{\max}. \tag{12}$$

The nondimensional time is defined such that we have full flood at $\tilde{t} = 0.25$ and full ebb at 0.75. The velocities are nondimensionalized by the tidal current amplitude U_t (Burchard et al. 2011) and the eddy viscosity by $H_{\max}$ and U_*:

$$\tilde{u} = u/U_t, \quad \tilde{v} = v/U_t, \quad \tilde{w} = w/U_t, \quad \text{and} \tag{13}$$

$$\tilde{A}_z = A_z/(H_{\max} U_*). \tag{14}$$

Residual (tidally averaged) values are denoted by triangular brackets, $\langle \tilde{u} \rangle$, and fluctuations by primes, $\tilde{u}' = \tilde{u} - \langle \tilde{u} \rangle$.

The estuarine circulation, that is, the total residual longitudinal circulation, is decomposed into contributions from tidal straining; gravitational and advectively driven circulation; and other, minor effects by means of the method presented by Burchard and Hetland (2010) and Burchard et al. (2011):

$$\langle \tilde{u}_{\text{total}} \rangle = \langle \tilde{u}_{\text{strain}} \rangle + \langle \tilde{u}_{\text{grav}} \rangle + \langle \tilde{u}_{\text{advec}} \rangle + \text{other}, \tag{15}$$

$$\langle u_i \rangle = \int_{-H}^{z} \mathcal{A}_i \, d\hat{z} - \frac{\gamma(y,z)}{H(y)} \int_{-H}^{0} \int_{-H}^{z} \mathcal{A}_i \, d\hat{z} \, dz, \quad \text{and} \tag{16}$$

$$\gamma(y,z) = \frac{H \displaystyle\int_{-H}^{z} \hat{z}/\langle A_z \rangle \, d\hat{z}}{\displaystyle\int_{-H}^{0} \int_{-H}^{z} \hat{z}/\langle A_z \rangle \, d\hat{z} \, dz}. \tag{17}$$

The tidal straining circulation $\langle \tilde{u}_{\text{strain}} \rangle$ results from the covariance of the eddy viscosity and the vertical shear of the longitudinal velocity divided by the residual viscosity:

$$\mathcal{A}_{\text{strain}} = -\langle A_z' \partial_z u' \rangle / \langle A_z \rangle. \tag{18}$$

The gravitational circulation $\langle \tilde{u}_{\text{grav}} \rangle$ is forced by the longitudinal buoyancy gradient and the advectively driven circulation $\langle \tilde{u}_{\text{advec}} \rangle$ by lateral and vertical advection:

$$\mathcal{A}_{\text{grav}} = \int_{z}^{0} \int_{\hat{z}}^{0} \langle \partial_x b \rangle \, d\tilde{z} \, d\hat{z} / \langle A_z \rangle, \quad \text{and} \tag{19}$$

$$\mathcal{A}_{\text{advec}} = \left(-\int_{z}^{0} \partial_y \langle uv \rangle \, d\hat{z} + \langle uw \rangle \right) \Big/ \langle A_z \rangle. \tag{20}$$

It should be noted that these contributions are not independent of each other but that they interact nonlinearly. For example, the tidal straining circulation is associated with stratification and shear, both of which are influenced by the total residual circulation. Still, the direct forcing mechanisms are identified with this method and can then be further investigated, as we will show for the tidal straining circulation [sections 4a(3) and 4b].

For the quantification of the intensity of the total circulation and its contributions, the following measure is applied (Burchard et al. 2011):

$$\mathcal{M}(\langle \tilde{u}_i \rangle) = -\frac{1}{W} \int_0^W \frac{4}{H^2(y)} \int_{-H(y)}^{0} \langle \tilde{u}_i \rangle (y,z) \left[z + \frac{H(y)}{2} \right] dz \, dy. \tag{21}$$

This measure is additive, that is,

$$\mathcal{M}(\langle \tilde{u}_{\text{total}} \rangle) = \mathcal{M}(\langle \tilde{u}_{\text{strain}} \rangle) + \mathcal{M}(\langle \tilde{u}_{\text{grav}} \rangle) + \mathcal{M}(\langle \tilde{u}_{\text{advec}} \rangle) + \text{other}, \tag{22}$$

and it preserves the orientation of the circulation, with $\mathcal{M}(\langle \tilde{u}_i \rangle) > 0$ for classical estuarine circulation.

For visualization of the transverse circulation, a particle tracking model is applied. The utilized integration scheme is fourth-order Runge–Kutta with a time step of $\Delta t = T/500 \approx 89.4$ s. The interpolation is linear in time and cubic in space. The model is implemented in MATLAB.

About 8000 particles are released in one-half of the cross section (symmetric, Fig. 1b). They are initially (at slack after ebb) distributed on a rectangular grid with a nondimensional spacing of $\Delta \tilde{z} = 6.7 \times 10^{-3}$ in the vertical and $\Delta \tilde{y} = 5 \times 10^{-3}$ in the lateral direction. (Note that the model is dimensional.) The particles are moved solely by transverse advection ($\tilde{v}$ and $\tilde{w}$) over one tidal cycle.

It should be noted that the transverse advection is not independent of the longitudinal advection ($\tilde{u}$). Only the direct influence of $\tilde{u}$ and of diffusion is ignored for the particle tracking.

4. Results and discussion

a. Aspect ratio and estuarine circulation

1) IMPACT OF THE ASPECT RATIO ON THE ESTUARINE CIRCULATION CONTRIBUTIONS

The impact of a channel's aspect ratio on the intensity of the estuarine circulation and its contributions is shown in Fig. 2. For convenience, we define the following three size classes: wide/shallow channels with $\alpha \leq \alpha_1 = 0.002$, narrow/deep channels with $\alpha \geq \alpha_2 = 0.015$, and medium channels in between. These limits (solid vertical lines in Fig. 2) coincide with distinct changes of the residual longitudinal circulation, particularly the tidal straining and the advectively driven contribution.

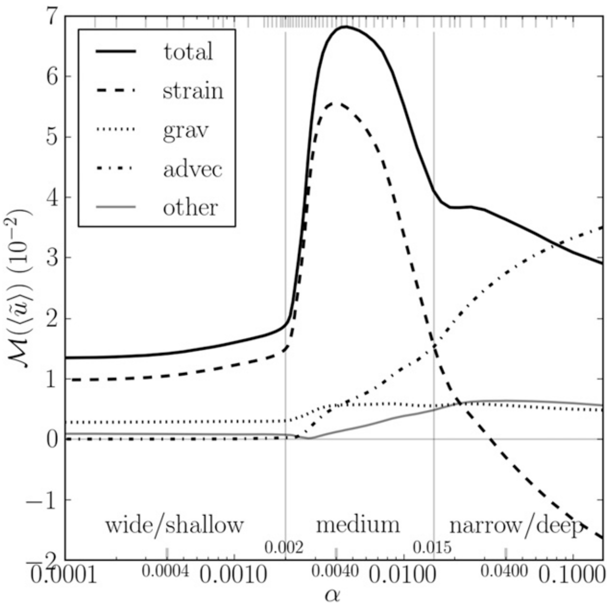

FIG. 2. Measure of the intensity of the residual longitudinal circulation contributions for varying aspect ratio (experiment A). The short bars at the upper abscissa mark the α values of the individual simulations; the two vertical lines represent the limits between wide, medium, and narrow channels ($\alpha_1 = 0.002$, $\alpha_2 = 0.015$); and the three short bars at the lower abscissa mark the channels shown in the following figures ($\alpha_w = 0.0004$, $\alpha_m = 0.004$, $\alpha_n = 0.04$).

It should be noted that the values of α_1 and α_2, as well as the course of the functions $\mathcal{M}(\langle\tilde{u}_i\rangle)$ over α, depend on the prescribed parameters (Table 1), which vary along real estuaries, just as α.

In wide channels, the estuarine circulation is relatively weak, with the tidal straining circulation being the dominant contribution (73%–79%), followed by the gravitational circulation (21%–16%).

At $\alpha_1 = 0.002$, the intensity of the tidal straining circulation starts to increase sharply, the advectively driven circulation starts to increase, and the gravitational circulation increases slightly. In medium channels, the total circulation reaches a maximum, which is caused primarily by a maximum of the tidal straining circulation at $\alpha_m = 0.004$. The advectively driven circulation continues to increase while the gravitational circulation remains about constant.

At $\alpha_2 = 0.015$, the advectively driven circulation becomes stronger than the tidal straining circulation so that, in narrow channels, the advectively driven circulation is the dominant contribution. The intensity of the tidal straining circulation falls below zero at $\alpha = 0.03$, that is, the tidal straining circulation reverses and opposes the classical estuarine circulation in very narrow channels. The gravitational circulation remains about constant.

These results raise the main question of this paper: Why is the tidal straining circulation maximum for a certain aspect ratio? Furthermore, why is it reverse in very narrow channels? Before we answer this [sections 4a(3) and 4b(1)], let us consider the residual velocity profiles establishing the circulation intensities.

2) COMPARISON OF RESIDUAL PROFILES FOR DIFFERENT ASPECT RATIOS

Cross-sectional views of the residual circulation contributions are shown in Fig. 3 for a wide ($\alpha_w = 0.0004$), a medium ($\alpha_m = 0.004$), and a narrow ($\alpha_n = 0.04$) channel. In agreement with the measure of their intensity (Fig. 2, α values marked at lower abscissa), the medium channel exhibits the strongest down-estuary residual flow at the surface and up-estuary flow above the bottom (Fig. 3a2), which is mainly caused by the strong tidal straining circulation (Fig. 3b2). The gravitational (Fig. 3c2) and the advectively driven contribution (Fig. 3d2) are much weaker.

In the wide channel, all circulation contributions are weaker than in the medium channel (Figs. 3a1,b1,c1,d1 versus Figs. 3a2,b2,c2,d2). The advectively driven circulation (Fig. 3d1) has almost ceased, so that the wide channel resembles a one-dimensional situation, that is, horizontal gradients are negligible (except for the prescribed longitudinal pressure gradients).

In the narrow channel, the advectively driven circulation is stronger than in the medium channel (Fig. 3d2 versus Fig. 3d3) and the tidal straining circulation exhibits up-estuary flow below the surface and down-estuary flow at the slopes and in the center of the channel (Fig. 3b3), which opposes the classical estuarine circulation [$\mathcal{M}(\langle\tilde{u}_{\text{strain}}\rangle) < 0$, Fig. 2].

Also shown in Fig. 3 are the residual eddy viscosity and the salinity. In the wide channel, salinity decreases from the thalweg to the shoals and only very slightly from the bottom to the surface (Fig. 3f1). Consequently, stratification is very weak. Eddy viscosity, on the other hand, is strong in the center of the channel (Fig. 3e1).

In the medium channel, salinity stratification is strong, with highest values above the center of the channel (Fig. 3e2). Eddy viscosity is relatively small and confined to the deep parts of the channel (Fig. 3f2).

In the narrow channel, salinity varies only very little, with strongest stratification occurring below the surface (Fig. 3f3). There, eddy viscosity is comparable to that in the medium channel; in the lower part, it is slightly higher (Fig. 3e3).

A detailed explanation of the differences in circulation, eddy viscosity, and stratification for

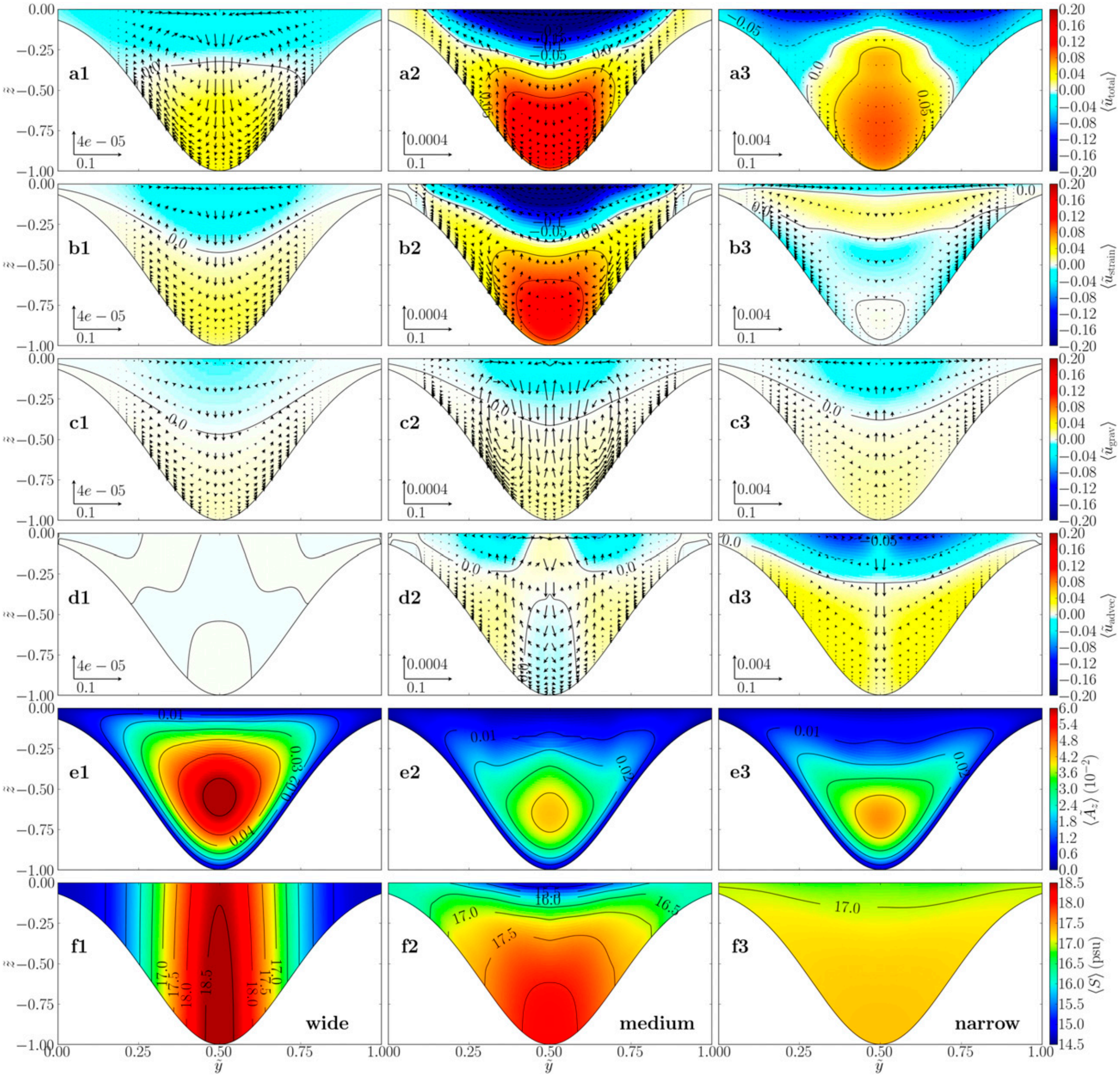

FIG. 3. (left) Wide ($\alpha_w = 0.0004$), (middle) medium ($\alpha_m = 0.004$), and (right) narrow ($\alpha_n = 0.04$) channel with residual profile of nondimensional (a) estuarine circulation, (b) tidal straining circulation, (c) gravitational circulation, (d) advectively driven circulation, (e) eddy viscosity, and (f) dimensional salinity. Note that the vertical velocity scale changes with the aspect ratio (see reference arrows).

different channel widths follows in sections 4a(3) and 4b.

3) Origin of the maximum and the reverse tidal straining circulation

To investigate the maximum of the tidal straining circulation in the medium channel, we now take a closer look at tidal cycles of the longitudinal velocity, its vertical shear, the eddy viscosity, the salinity, the Brunt–Väisälä frequency, and the gradient Richardson number at the thalweg (Fig. 4). Recall that the covariance of viscosity and vertical shear of longitudinal velocity divided by residual viscosity is the driving term for the tidal straining circulation [$\mathcal{A}_{\text{strain}}$, (18)].

In the wide channel, the expected behavior of weak, strain-induced periodic stratification is observed (SIPS; see section 1a and references therein): the shear is weakly asymmetric, with negative shear being slightly stronger and longer lasting than positive shear ($\partial_z \tilde{u} \approx -1.08$ at full

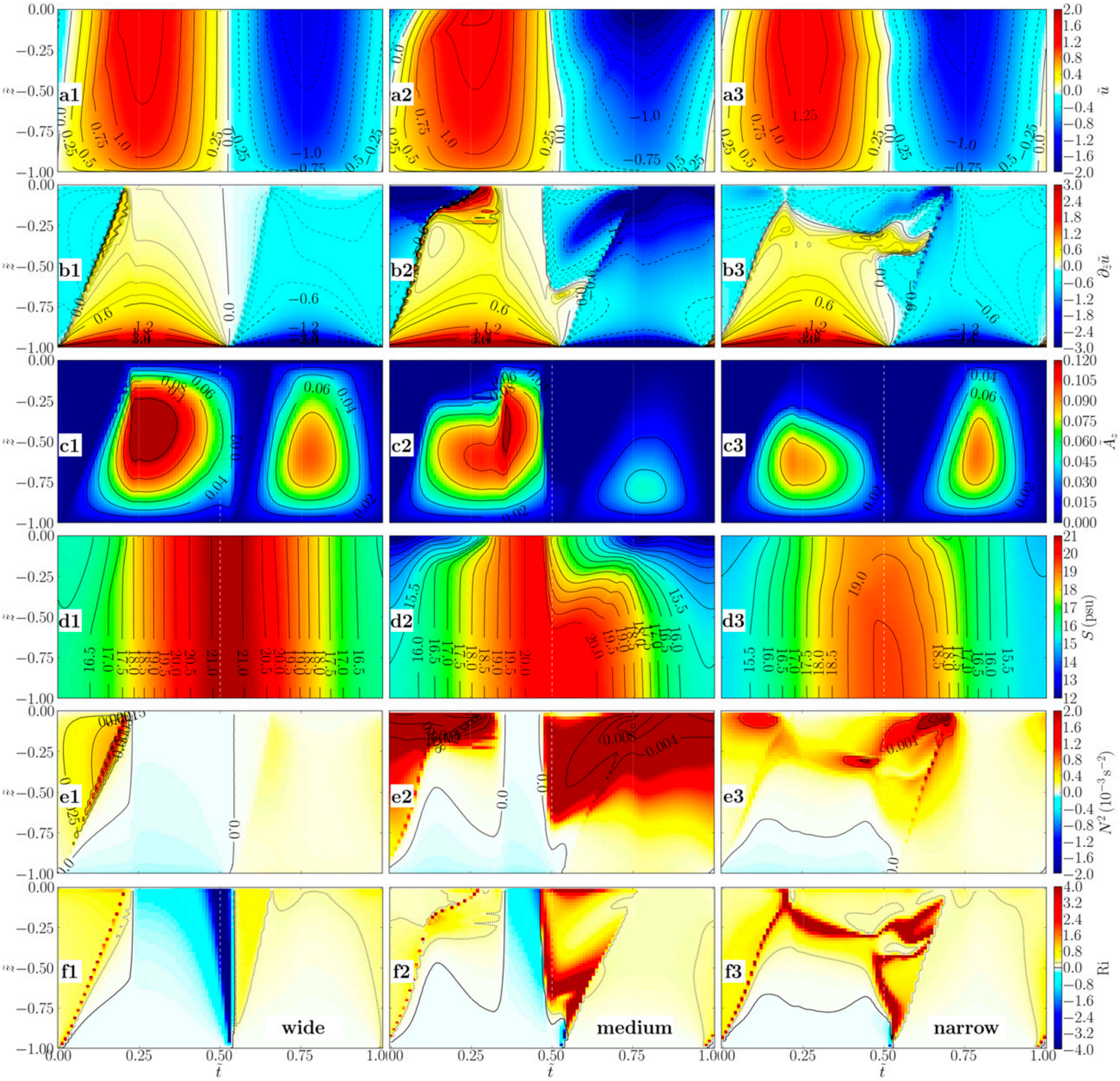

FIG. 4. (left) Wide ($\alpha_w = 0.0004$), (middle) medium ($\alpha_m = 0.004$), and (right) narrow ($\alpha_n = 0.04$) channel with tidal cycle at thalweg of nondimensional (a) longitudinal velocity, (b) vertical shear of longitudinal velocity, (c) eddy viscosity, (d) dimensional salinity, (e) dimensional Brunt–Väisälä frequency, and (f) gradient Richardson number (solid contour at Ri = 0, dotted at 0.25; see section 1a).

ebb versus 1.03 at full flood, thalweg averages; Figs. 4a1,b1). This is because of the eddy viscosity asymmetry with smaller eddy viscosity during ebb than during flood (Fig. 4c1), which is again due to the weak, strain-induced stratification during ebb and early flood and homogeneous or even unstable water columns (negative N^2 and Ri) during full and late flood (Figs. 4d1,e1,f1).

The tidal asymmetries grow drastically when going to medium channels. (Recall that only the aspect ratio is changed, in terms of nondimensional numbers.) In the medium channel, negative shear is much stronger than the positive shear (−1.99 versus 1.24), particularly in the upper half of the thalweg water column (−1.14 versus 0.31; Figs. 4a2,b2). This leads to very high shear fluctuations with $\partial_{\tilde{z}}\tilde{u}' < 0$ (i.e., $\partial_{\tilde{z}}\tilde{u} < \partial_{\tilde{z}}\langle\tilde{u}\rangle$) during ebb and $\partial_{\tilde{z}}\tilde{u}' > 0$ (i.e., $\partial_{\tilde{z}}\tilde{u} > \partial_{\tilde{z}}\langle\tilde{u}\rangle$) during flood (not shown). Furthermore, negative shear is very persistent in the upper half, at the surface even from before slack after flood ($\tilde{t} \approx 0.47$) until after full flood ($\tilde{t} \approx 0.27$). This strong and long-lasting negative shear is due to very

TABLE 3. Overview of the characteristics leading to maximum tidal straining circulation as well as their fulfilment (☑) for the three size classes. [An empty check box, ☐, corresponds to the notation (¬*i*), etc., in the text.]

	Fulfilment of characteristics	Wide	Medium	Narrow
(i)	$\partial_z\tilde{u}' > 0$, $\tilde{A}_z' > 0$ during flood	☑	☑	☐
(ii)	$\partial_z\tilde{u}' < 0$, $\tilde{A}_z' < 0$ during ebb	☐	☑	☐
(iii)	$\langle\tilde{A}_z\rangle$ small	☐	☑	☑

low eddy viscosity not only during ebb (Fig. 4c2): eddy viscosity strongly decreases already before slack after flood, remains comparably low even at full ebb, and peaks only after full flood ($\tilde{t} \approx 0.36$). This low eddy viscosity is again due to very strong stratification (Figs. 4d2,e2,f2), which sets in already before slack after flood and persists throughout the entire ebb phase and into the flood phase, at the surface even until after full flood. This behavior cannot be explained by the longitudinal tidal currents; transverse processes must play an important, stratifying role and are going to be investigated in section 4b(1).

In the narrow channel, negative shear is still stronger and longer lasting than positive shear (−1.14 versus 1.03) (Figs. 4a3,b3). Close to the surface, this negative shear even persists over the entire tidal cycle. Eddy viscosity is now stronger during ebb than during flood (Fig. 4c3), but its maximum is smaller than that in wide or medium channels. This reverse eddy viscosity asymmetry is due to a reverse stratification pattern with strongest (though still weak) stratification during and shortly after flood and homogeneous water columns in the second half of the ebb phase (Figs. 4d3,e3,f3). This behavior cannot be explained by the longitudinal tidal currents either.

Three characteristics lead to the observed maximum of the tidal straining circulation in the medium channel (Table 3): (i) positive shear fluctuation ($\partial_z\tilde{u}' > 0$) coincides with strong eddy viscosity, that is, positive viscosity fluctuation ($\tilde{A}_z' > 0$; i.e., $\tilde{A}_z > \langle\tilde{A}_z\rangle$), during flood; (ii) negative shear fluctuation coincides with very weak eddy viscosity, that is, negative viscosity fluctuation, during ebb; and (iii) the residual eddy viscosity is low. Characteristics (i) and (ii) determine the orientation of the tidal straining circulation, which is classical [$\mathcal{M}(\langle\tilde{u}_{\text{strain}}\rangle) > 0$] in the medium channel. All three characteristics determine the intensity, which shows a maximum value here.

In the wide channel, only characteristic (i) is clearly fulfilled; positive shear fluctuation coincides with strong viscosity fluctuation during flood. Negative shear fluctuation coincides with moderate viscosity, that is, positive viscosity fluctuation (not shown), around full ebb [(ii) not fulfilled, indicated as (¬ii)]; however, negative shear fluctuation coincides with very weak viscosity, that is, negative viscosity fluctuation, at the beginning of ebb and around slack after ebb (ii). The residual tidal straining circulation in the wide channel is classically oriented, but the opposing contribution during ebb (¬ii) and the high residual viscosity (¬iii) yield a weak intensity.

In the narrow channel, the eddy viscosity asymmetry is reverse, but the shear asymmetry is not. (The surface shear is negative during flood, but its fluctuation is positive like in wide and medium channels; not shown.) Positive shear fluctuation coincides with moderate viscosity, that is, positive viscosity fluctuation, around full flood (i) but with very weak viscosity, that is, negative viscosity fluctuation, at the beginning and end of flood (¬i). Negative shear fluctuation coincides with very weak viscosity, that is, negative viscosity fluctuation, at the beginning and end of ebb (ii) but with strong viscosity, that is, positive viscosity fluctuation, around full ebb (¬ii). The classical-opposing contributions are slightly larger than the classical so that the residual tidal straining circulation opposes the classical orientation, that is, the tidal straining circulation is reverse in narrow channels. The fact that these contributions almost balance yields a weak intensity even though the residual viscosity is low (iii).

b. Transverse stratifying and destratifying processes

1) STRATIFICATION BY TRANSVERSE SALINITY ADVECTION

As explained above, the vertical shear of the longitudinal velocity is affected by the eddy viscosity, which itself is affected by the stratification. The observed change of the stratification pattern with only the aspect ratio (Figs. 4d1,d2,d3,e1,e2,e3) suggests the importance of transverse, stratifying as well as destratifying processes. To understand these processes, we now consider the lateral and vertical advection of salinity over one tidal cycle. Figure 5 shows snapshots of the lateral velocity and the salinity.

We begin with the medium channel and the flood phase. The slope $\partial_y H(y)$ causes laterally differential longitudinal advection of salinity, which builds a lateral salinity gradient with highest salinity at the thalweg (Figs. 5b2,c2,d2,e2). This generates flood-oriented transverse circulation (surface convergence) (Figs. 5c2,d2,e2), which strains the salinity field (Figs. 5d2,e2) and induces strong stratification already shortly before slack after flood (Fig. 5e2).

The strong stratification in the center of the channel persists throughout the ebb and into the flood phase

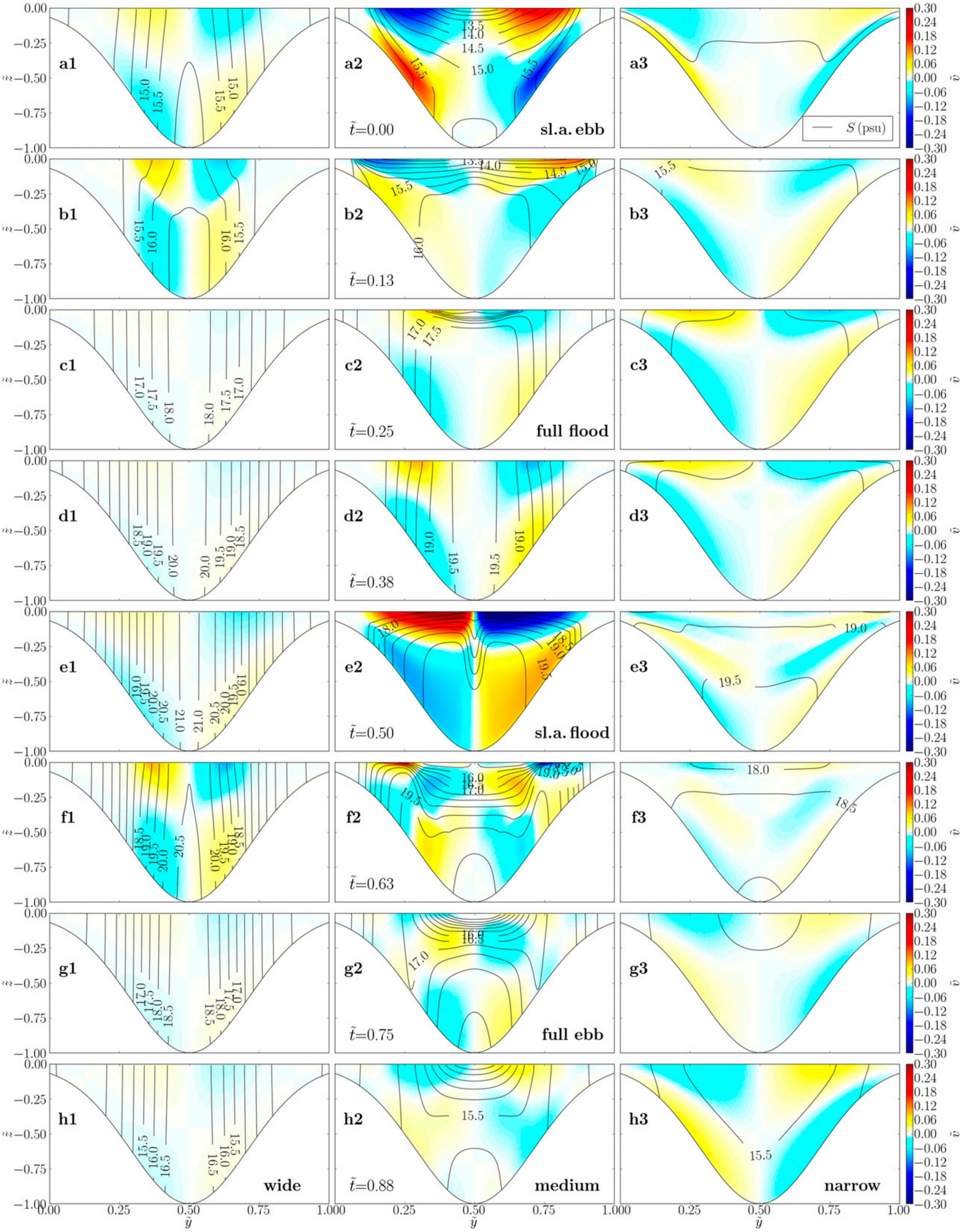

FIG. 5. (left) Wide ($\alpha_w = 0.0004$), (middle) medium ($\alpha_m = 0.004$), and (right) narrow ($\alpha_n = 0.04$) channel with lateral velocity (color) and salinity (contours, interval 0.5 psu) at (a) $\tilde{t} = 0.00$ (slack after ebb), (b) 0.13, (c) 0.25 (full flood), (d) 0.38, (e) 0.50 (slack after flood), (f) 0.63, (g) 0.75 (full ebb), and (h) 0.88.

(Figs. 5e2,f2,g2,h2,a2,b2,c2). Laterally differential longitudinal advection during ebb builds a salinity gradient with lowest salinity at the thalweg, in the upper half of the cross section (Figs. 5g2,h2,a2). This generates ebb-oriented transverse circulation (Figs. 5h2,a2,b2), which also enhances stratification (Figs. 5a2,b2).

Considering the effect of stratification on eddy viscosity and thus vertical shear of horizontal velocities, the key leading to the maximum of the tidal straining circulation in the medium channel appears to be the matching length scales of half the channel width and the lateral salinity advection during the second half of flood (Figs. 5c2,d2,e2), which leads to strong stratification already at the very beginning of the ebb phase (Fig. 5e2). Because of the stratification-shear feedback during ebb (enforcing each other until the gradient Richardson number Ri falls below 0.25, at the surface around full ebb; Fig. 4f2), the ebb viscosity is very low and thus the tidal asymmetry very strong.

The wide channel has a gentler slope so that the lateral gradients of the longitudinal velocity and thus of the salinity are smaller than in the medium channel. (Note that the salinity range over $\tilde{y}$ needs to be 10 times as large as in the medium channel to imply the same lateral salinity gradient.) Consequently, the transverse circulation is weaker so that, also considering the larger width, the salinity field is hardly strained (Figs. 5a1,b1,f1). Furthermore, the lateral salinity gradient and the transverse circulation are always flood oriented. This is because of the positive feedback of the lateral gradients and the transverse circulation during flood (see Lerczak and Geyer 2004) and the high inertia of the large water body.

The narrow channel has a steeper slope so that the lateral gradients of the longitudinal velocity and thus of the salinity are larger than in the medium channel. (Note that the salinity range over $\tilde{y}$ is much smaller than in the medium channel, but not by a factor of 10.) Consequently, the transverse circulation is stronger so that, also considering the smaller width, the salinity field is strained very fast, that is, already before full flood (Figs. 5b3,c3). This fast straining leads to persistent stratification at the surface (Figs. 4d3,e3) and thus to low eddy viscosity and negative shear during flood (Figs. 4c3, b3). (It should be noted that the overall stratification in the narrow channel is substantially weaker than in the medium channel.) During ebb, longitudinal SIPS adds (Fig. 5f3), but the stratification-shear feedback (see above) leads to $\mathrm{Ri} < 0.25$ already before full ebb (Fig. 4f3), so that stratification is reduced by strong shear production of turbulence and the eddy viscosity is higher than during flood. This reverse stratification and eddy viscosity asymmetry leads to the reverse tidal straining circulation.

2) DISTINCTION OF THE STRATIFYING PROCESSES: PARTICLE TRACKING AND MATHEMATICAL DECOMPOSITION

Figure 5 clearly suggests but cannot prove that transverse salinity advection is the dominant stratifying process in the medium channel. By means of particle tracking, the contribution of transverse advection to the salinity redistribution can be visualized.

The results of the transverse particle tracking are presented in Fig. 6 for the second half of flood. Shown are the instantaneous positions of the particles, marked by dots, and their color-coded salinity (see below and figure caption). The initially equidistant particle distribution (at slack after ebb, not shown) becomes inhomogeneous because of interpolation and truncation errors of the integration scheme. (Note that there is no convergence or divergence in the transverse plane, $\partial_y v + \partial_z w = 0$ since $\partial_x u = 0$.) For the color mapping of the particles (Fig. 6), we use the following salinity fields:

- Fig. 6a - instantaneous, that is, at present position and time (full flood, contours in Fig. 5c);
- Fig. 6b - memorized, that is, at previous position and time (full flood, particles as information carrier); and
- Fig. 6c - instantaneous (slack after flood, Fig. 5e).

Thus, Fig. 6b shows the hypothetical salinity at slack after flood for the theoretical case that the salinity at full flood (Fig. 6a) is solely advected by transverse circulation, that is, that longitudinal advection and salinity diffusion are ignored. (Please note again that only their direct influence on the particles is ignored; they still codetermine the transverse circulation.) Figure 6c shows the actual salinity at slack after flood as it results from longitudinal and transverse advection, diffusion, and their interaction.

The wide channel is vertically homogeneous at full flood with salinity increasing toward the thalweg (Fig. 6a1). The generated transverse circulation induces very weak stratification above the slopes at slack after flood (Fig. 6b1). Comparison of Fig. 6b1 with Fig. 6c1 indicates that this is the dominant stratifying process in this part of the tidal cycle.

The medium channel is also vertically homogeneous at full flood with salinity increasing toward the thalweg, except for subsurface stratification at the thalweg (Fig. 6a2), which is a remainder from strong stratification during ebb (Figs. 4d2,e2). The transverse circulation induces strong stable stratification at slack after flood, except for the thalweg and the bottom at the

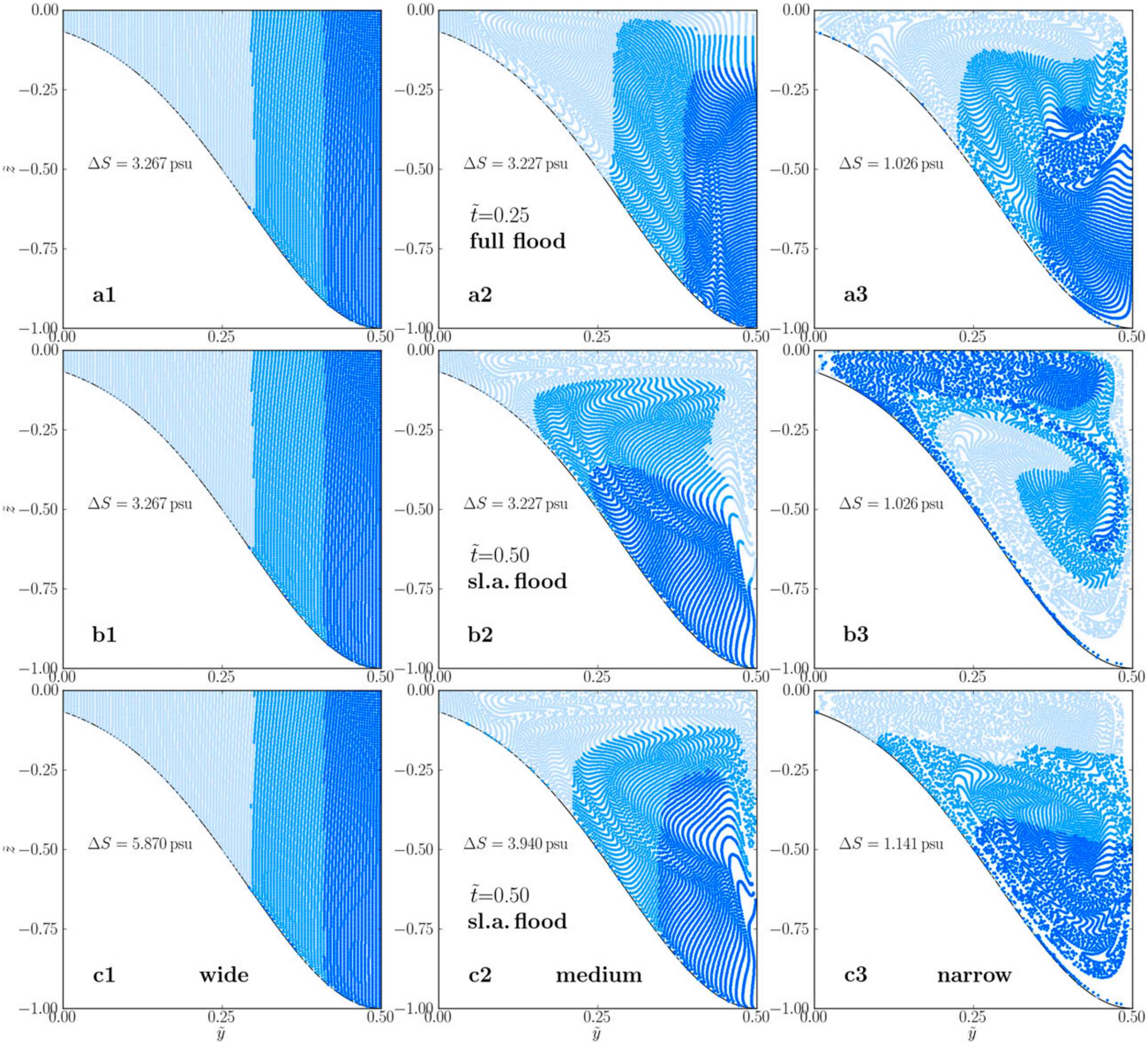

FIG. 6. (left) Wide (α_w = 0.0004), (middle) medium (α_m = 0.004), and (right) narrow (α_n = 0.04) channel with (a) salinity at full flood (cf. contours in Fig. 5c), (b) hypothetical salinity at slack after flood if the salinity at full flood (a) is solely advected by transverse circulation (particle tracking), and (c) actual salinity at slack after flood (cf. Fig. 5e). The dots mark the particle positions at the given time. Their blue shadings indicate the freshest (light blue), middle, and saltiest third (deep blue) of the particles. (The salinity range ΔS is given in each panel.)

slopes (Fig. 6b2). Comparison of Fig. 6b2 with Fig. 6c2 indicates that this is the dominant stratifying process here, too. The actual salinity field (Fig. 6c2) is vertically homogeneous above the bottom at the slopes because of turbulent diffusion and more saline toward the thalweg because of further laterally differential longitudinal advection.

The narrow channel is already weakly stratified in the upper center of the channel at full flood (Fig. 6a3). The transverse circulation stirs the salinity field and induces unstable stratification at slack after flood (Fig. 6b3). The actual salinity field (Fig. 6c3) is not unstable, though, but stably stratified because of the negative shear close to the surface even during flood [section 4a(3), Fig. 4b3].

Stratification by transverse salinity advection is composed of lateral and vertical straining and advection of stratification. The contributions from longitudinal, lateral, and vertical straining and advection to the stratification can be distinguished when considering the residual of the vertical gradient of the salinity budget [(A3)]:

$$
\begin{aligned}
0 &= \langle \cancel{\partial_t \partial_z S} \rangle + \langle \partial_z (u \partial_x S) \rangle + \langle \partial_z (v \partial_y S) \rangle + \langle \partial_z (w \partial_z S) \rangle \\
&\quad - \langle \partial_z \partial_{y*} (K_{y*} \partial_{y*} S) \rangle - \langle \partial_z \partial_z (K_z \partial_z S) \rangle \\
&= \underbrace{\langle \partial_z u \partial_x S \rangle}_{\substack{\text{long.strain.} \\ \rightarrow \text{1SIPS}}} + \underbrace{\langle \partial_z v \partial_y S \rangle}_{\substack{\text{lat.strain.} \\ \rightarrow \text{2SIPS}}} + \underbrace{\langle \partial_z w \partial_z S \rangle}_{\substack{\text{vert.strain.} \\ \rightarrow \text{3SIPS}}} \\
&\quad + \cancel{\underbrace{\langle u \partial_x \partial_z S \rangle}_{\substack{\text{long.advec.} \\ \rightarrow \text{1APS}}}} + \underbrace{\langle v \partial_y \partial_z S \rangle}_{\substack{\text{lat.advec.} \\ \rightarrow \text{2APS}}} + \underbrace{\langle w \partial_z \partial_z S \rangle}_{\substack{\text{vert.advec.} \\ \rightarrow \text{3APS}}} \\
&\quad - \underbrace{\langle K_{y*} \partial_{y*} \partial_{y*} \partial_z S \rangle}_{\text{quasi}-\text{lat.diff.}} - \underbrace{\langle \partial_z \partial_z (K_z \partial_z S) \rangle}_{\text{vert.diff.}} ;
\end{aligned}
\tag{23}
$$

$K_z(y, z, t)$ is the vertical diffusivity of salinity. [Note that $\partial_x S$ and K_{y*} are constant here (see section 3b), that is, $\partial_x \partial_z S = 0$ (vanishing longitudinal advection), and $\partial_{y*} \partial_z K_{y*} = 0$.]

Without the residual, (23) is similar to the evolution equation of stratification in Giddings et al. [2011, their (7)] and provides an alternative to the evolution equation of potential density anomaly (Burchard and Hofmeister 2008; de Boer et al. 2008).

Since longitudinal SIPS is a universal process in all regions with longitudinal density gradients and tidal currents, we call it primary strain-induced periodic stratification (1SIPS) in the following. Accordingly, we suggest calling periodic stratification by lateral/vertical straining secondary/tertiary strain-induced periodic stratification (2/3SIPS).

Laterally/vertically advected periodic stratification is abbreviated 2/3APS. The combination of APS and SIPS is already known as ASIPS (de Boer et al. 2008; Howlett et al. 2011), in our case 2ASIPS for laterally and 3ASIPS for vertically advected and strain-induced periodic stratification.

All terms in (23) are nondimensionalized by multiplication with $H_{\max}/(U_* |\partial_x S|) > 0$. The residual and cross-sectionally averaged nondimensional straining, advection of stratification, and vertical diffusion are shown in Fig. 7 (positive ≡ stratifying). (The quasi-lateral diffusion term is negligible and therefore omitted.)

In wide channels (without Coriolis forcing), 1SIPS is more important than 2- and 3ASIPS. In very wide channels, 2- and 3ASIPS are negligible.

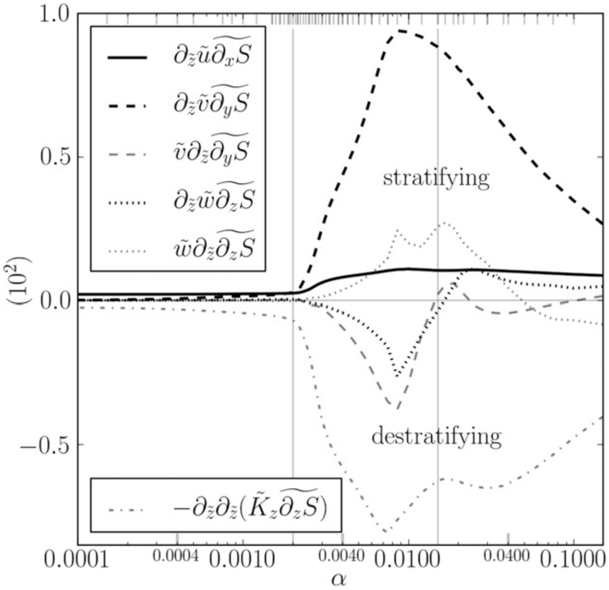

FIG. 7. Residual and cross-sectionally averaged nondimensional stratifying (>0) and destratifying terms (23). Vertical lines and bars as in Fig. 2.

In medium channels, 1SIPS is about 4 times as strong as in wide channels (feedback of transverse processes), but 2SIPS increases and dominates considerably, though it is partly compensated by negative 2APS, that is, lateral advection of weaker stratification (from shoals to thalweg, not shown). Negative 3SIPS and positive 3APS approximately balance each other.

In narrow channels, 2SIPS is still the dominant stratifying term, but it decreases. Positive 3SIPS contributes about half as strong as 1SIPS. Close to the limit between medium and narrow channels ($\alpha \approx 0.02$), 3SIPS and positive 3APS, that is, vertical advection of stronger stratification (from surface to bottom, not shown), concur so that 3ASIPS is about 3 times as important as 1SIPS.

3) SECONDARY STRAIN-INDUCED PERIODIC STRATIFICATION

Since 2SIPS is the dominant stratifying term except in wide channels (Fig. 7), it is now elucidated a bit further. It has a periodicity of $T/2$: in the medium channel, transverse circulation is generated (or rather turned into the orientation corresponding to the respective tidal phase) around full tides (Figs. 5c2,h2), when laterally differential longitudinal advection has already built a considerable lateral salinity gradient (schematic Fig. 8a; cf. Figs. 6a1,a2). As soon as lateral straining has flattened this gradient, stratification is maximum (Fig. 8b2). In the medium channel, this occurs around slack tides (Figs. 5b2,e2, 6b2).

The further development depends on the tidal phase. After slack after ebb, during the first half of flood, stratification is decreased (Figs. 5b2,c2,d2); after flood, during ebb, it is increased (Figs. 5e2,f2,g2) because of 1SIPS (periodicity T).

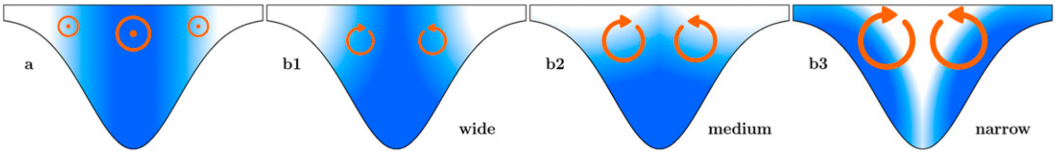

FIG. 8. Schematic of secondary straining: (a) laterally differential longitudinal advection (orange arrowheads; figure orientation: looking down-estuary) and lateral salinity gradient (deeper blue shading indicates higher salinity) during flood and (b) transverse circulation and strained salinity field in (b1) wide, (b2) medium, and (b3) narrow channels at slack after flood.

In addition to multidirectional SIPS and APS, shear-induced turbulence (periodicity $T/2$) interferes with the stratification (highest shear, turbulent diffusion, and destratification at full tides; cf. Fig. 4). Furthermore, all these processes interact nonlinearly so that it is difficult to distinguish the effect of 2SIPS.

In wider channels, 2SIPS is weaker and limited to the slopes (Figs. 5a1,b1,f1, 6b1) because the length scale of the lateral velocity is smaller than half the channel width (Fig. 8b1). Lateral straining and stratification are maximum only after slack tides (Figs. 5b1,f1).

In narrower channels, 2SIPS sets in very early (Figs. 5b3,f3, 6a3) and is then subject to longitudinal shear (Figs. 4a3,b3) and turbulent diffusion (Figs. 6b3,c3). The length scale of the lateral velocity is larger than half the channel width so that transverse stirring occurs (Fig. 8b3; cf. Fig. 6b3).

c. *Further results and discussion*

1) IMPORTANCE OF TRANSVERSE ADVECTION OF SALINITY AND MOMENTUM

Further evidence of the importance of transverse salinity advection for the maximum of the tidal straining circulation is provided by comparison of the full-physics experiment (A) with reduced experiments ignoring transverse advection of momentum (C), of salinity (F), and of both (D; no lateral internal pressure gradient, i.e., no transverse circulation). The maximum of the tidal straining circulation still exists in experiment C but not in experiments D and F (Fig. 9a). This implies that salinity advection is more important for the phenomenon than momentum advection.

In experiment D, the intensity of the tidal straining circulation is constant over α, as expected: without lateral internal pressure gradients, transverse processes are completely switched off so that the lateral dimension does not play a role. The intensities of all circulation contributions in experiment A (Fig. 2) remain constant at the values of experiment D (Fig. 9a) for $\alpha \lesssim 0.0003$ because then the slope $\partial_y H$ is too small to cause significant lateral gradients of salinity and velocity. Thus, transverse processes are negligible (quasi one-dimensional).

The maximum of the tidal straining circulation is due to a maximum of the viscosity–shear covariance in medium channels [$\alpha \approx \alpha_m = 0.004$; Fig. 9b, experiments A and C; characteristics (i) and (ii) in section 4a(3)] as well as to a decrease of the residual eddy viscosity around the limit between wide and medium channels [$\alpha_1 = 0.002$; Fig. 9c; characteristic (iii); also see (18)].

2) GENERALITY OF THE RESULTS

To substantiate the generality of our findings, we carry out further simulations (experiment A) with different prescribed parameters, namely, a nonzero Coriolis parameter, $f = 1 \times 10^{-4}\,\mathrm{s}^{-1}$ (inverse Ekman number $\mathrm{E}_i = fH/U_* = 0.045$; Fig. 10a); a depth profile with steeper slopes and wider shoals, $\lambda = 0.75$ (dashed line in Fig. 1b; Fig. 10b); and half the longitudinal salinity gradient, $\partial_x S = -1.5\,\mathrm{psu\,m^{-1}}$ (Si = 0.24; Fig. 10c).

The intensities of the circulation contributions in these simulations are weaker (note the different $\mathcal{M}$ scales) and the maxima of the tidal straining circulation and the estuarine circulation are shifted, compared to the reference simulation (Fig. 2). However, the qualitative behavior is in very good agreement with the described impact of the aspect ratio on the estuarine circulation.

With Coriolis force (Fig. 10a), the intensity of the total residual and of the tidal straining circulation shows a reduction by about 20% (cf. Fig. 2) in the medium α range. The rotationally driven contribution $\langle \tilde{u}_{\mathrm{rot}} \rangle$ (see Burchard et al. 2011) is insignificant. This can be understood when considering the importance of friction relative to the local acceleration [see, e.g., Winant 2008, their (A7)]:

$$\delta = \sqrt{2\langle A_z \rangle/(\omega H_{\max}^2)} = \sqrt{2\langle \tilde{A}_z \rangle/\mathrm{Un}}. \tag{24}$$

With $\langle \tilde{A}_z \rangle$ from Fig. 9c, (24) yields $\delta \approx 1.2$ (0.9) for the wide (medium, narrow) channel, that is, large friction and negligible Coriolis force.

Furthermore, we cover the two-dimensional parameter space spanned by medium aspect ratios and low-to-moderate Simpson numbers (about 90 simulations; Fig. 11). Note that runaway stratification occurs for higher Si,

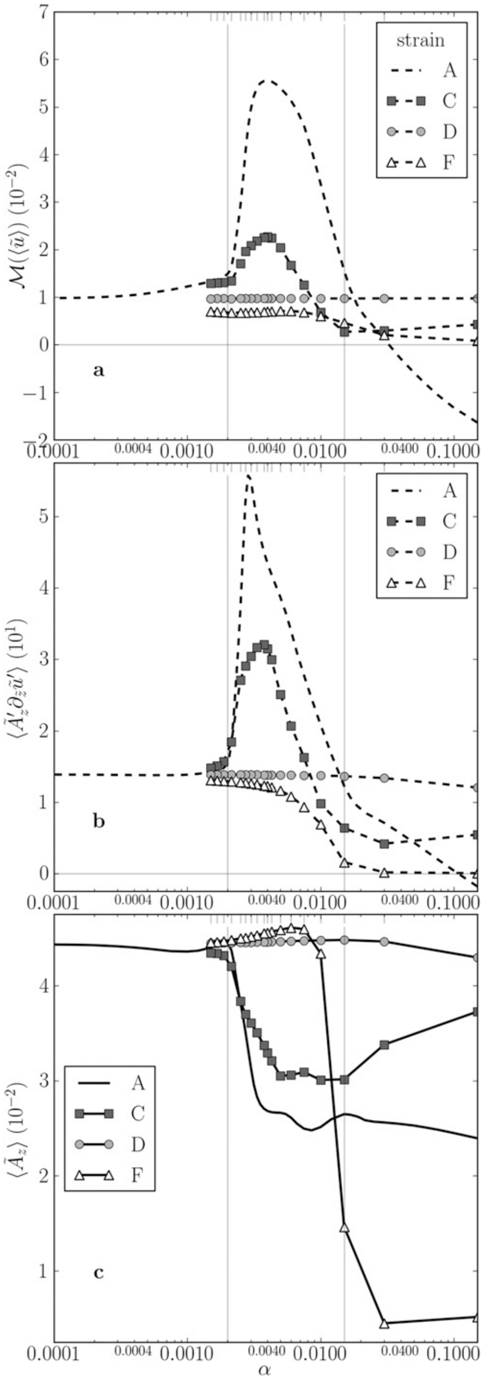

FIG. 9. Comparison of full and reduced experiments (A, full physics; C, no momentum advection; D, no lateral internal pressure gradient; F, no transverse salinity advection): (a) as in Fig. 2, but only tidal straining circulation, and thalweg average of nondimensional (b) viscosity–shear covariance and (c) residual eddy viscosity. The short bars at upper abscissa mark the α values of the individual reduced experiments; vertical lines as in Fig. 2.

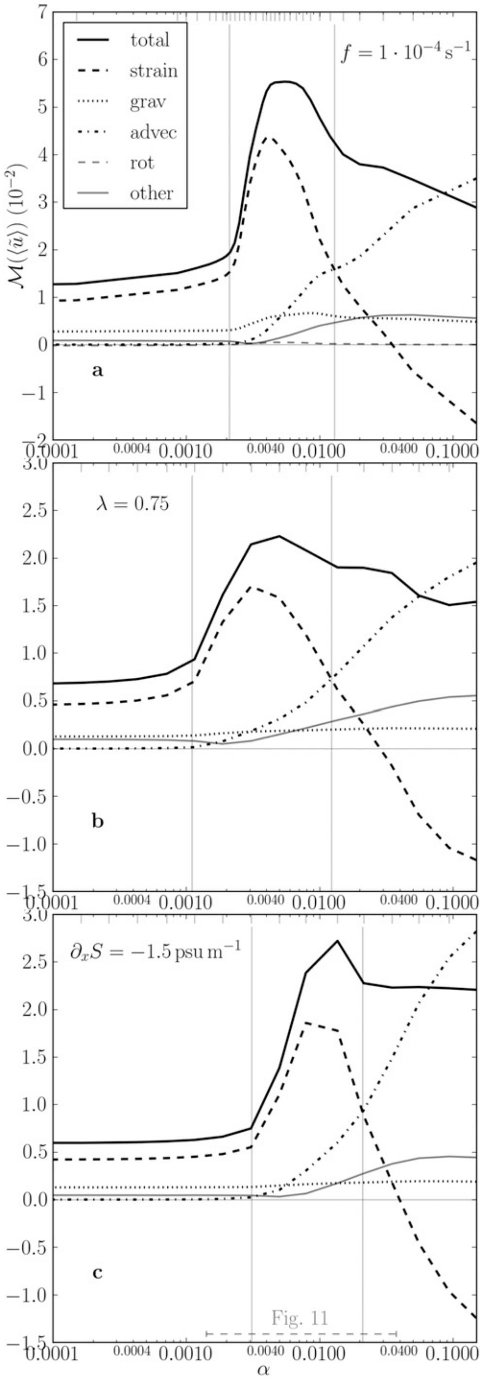

FIG. 10. As in Fig. 2, but with different prescribed (a) Coriolis parameter, (b) depth profile, and (c) salinity gradient.

a common problem of one- and two-dimensional simulations (Geyer and MacCready 2014).

For decreasing Si, the intensity of the tidal straining circulation decreases (Fig. 11; cf. Burchard et al. 2011, 2014) and the maximum is shifted to narrower channels. The aspect ratio of the channel with maximum tidal

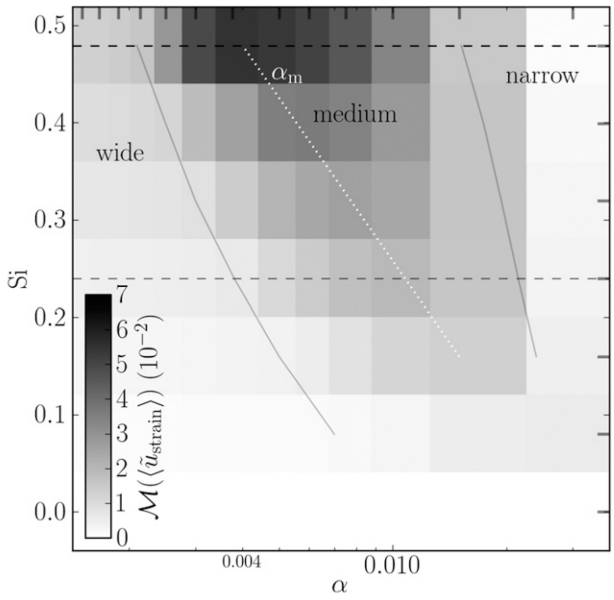

FIG. 11. Intensity of the tidal straining circulation in the 2D parameter space spanned by α and Si. The short bars at the upper abscissa and at the right ordinate mark the α and Si values of the individual simulations. The gray solid lines represent the limits between wide, medium, and narrow channels [see section 4a(1)]; the white dotted line connects the maxima per Si. The black dashed line corresponds to Fig. 2; the gray dashed line corresponds to Fig. 10c (α range marked at lower abscissa there).

straining circulation appears to depend exponentially on the Simpson number: $\alpha_m \propto \exp(-\mathrm{Si})$ (white dotted line; note the logarithmic α scale in all figures). Assuming constant H, this can be rewritten as $W_m \propto \exp(\mathrm{Si})$.

A lower Si is equivalent to a smaller longitudinal salinity gradient, which via laterally differential longitudinal advection implies a smaller lateral salinity gradient. This leads to a weaker transverse circulation so that the secondary strain-induced periodic stratification, and thus the intensity of the tidal straining circulation, is maximum in a narrower channel. This functional chain is highly nonlinear, though, for example, because Si also affects the longitudinal gravitational circulation and the background stratification.

In a final step, we carry out three-dimensional simulations with nonzero river discharge and free surface elevation (appendix B). These simulations qualitatively confirm the results obtained with the simplified two-dimensional model (cf. Figs. 2 and A1b).

Please note that the qualitative impact of the aspect ratio on lateral gradients (of H, u, S), on 2SIPS, and thus on the intensity of the tidal straining circulation, is of general nature, though we (can) cover only a small part of the parameter space to prove this. It should be noted again that the results presented in this paper apply to periodically, weakly stratified estuaries. In a permanently stratified estuary, for example, lateral straining probably has a much weaker additional effect on the stratification.

3) A NOTE ON STRATIFICATION AND MIXING

Stratification decreases the eddy viscosity A_z and thus the mixing of momentum (see section 1a). It also decreases the eddy diffusivity K_z, but not the mixing of salinity; this increases with stratification [(27)]. It should be noted that K_z is decreased more than A_z in a stably stratified water column, that is, the turbulent Prandtl number is larger than one, $\mathrm{Pr} = A_z/K_z > 1$ (Kundu and Cohen 2002).

The strength of stratification, that is, the stability of a water column, can be measured by means of the potential density anomaly (e.g., Simpson et al. 1981; Burchard and Hofmeister 2008; de Boer et al. 2008),

$$\phi = 1/H \int_{-H}^{0} (\overline{\rho} - \rho) g z \, dz , \qquad (25)$$

where $\overline{\rho}$ is the vertically averaged density. We nondimensionalize as follows:

$$\tilde{\phi} = \phi/(\rho_0 g H_{\max}) = 1/(H H_{\max}) \int_{-H}^{0} (\overline{\rho} - \rho)/\rho_0 z \, dz , \qquad (26)$$

where ρ_0 is the reference density (see section 2a).

According to Burchard et al. (2009) and Becherer and Umlauf (2011), vertical mixing of salinity can be defined as

$$\chi_z^S = 2K_z(\partial_z S)^2 . \qquad (27)$$

We nondimensionalize as follows [cf. (14)]:

$$\tilde{\chi}_z^S = \chi_z^S/[H_{\max} U_* (\partial_x S)^2] = 2\tilde{K}_z(\partial_z S/\partial_x S)^2 . \qquad (28)$$

The residual and cross-sectionally averaged nondimensional potential density anomaly and vertical mixing are shown in Fig. 12. They behave very similarly, that is, both stratification and vertical mixing are weak in wide, strong in medium, and moderate in narrow channels. They are maximum at the same aspect ratio as the intensity of the tidal straining circulation (Fig. 2; $\alpha_m = 0.004$).

5. Conclusions

Generally, stratification in an estuary is induced by the vertical shear of the longitudinal ebb currents

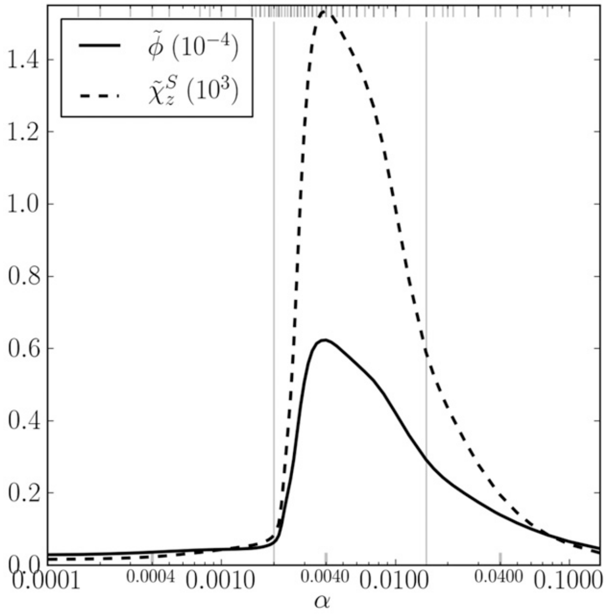

FIG. 12. Residual and cross-sectionally averaged nondimensional potential density anomaly [(26)] and vertical mixing of salinity [(28)]. Vertical lines and bars as in Fig. 2.

(faster and thus fresher at the surface) and increased during the ebb phase (longitudinally, primary strain-induced periodic stratification, 1SIPS). However, the surface-convergent transverse circulation during flood can induce stratification too (mainly laterally, secondary, 2SIPS): it transports fresher water from the shoals (fresher there because of laterally differential longitudinal advection) to the thalweg, at the surface, and spreads the saltier water from the thalweg in the deep channel and along the bottom of the slopes. For a certain, medium aspect ratio ($\alpha \approx 0.004$ for our set of nondimensional numbers), the two bodies of fresher water just merge at the thalweg (at the surface) at slack after flood, so that the stratification is very strong already at the beginning of the ebb phase.

It should be noted that the dominance of 2SIPS over 1SIPS in medium and narrow channels implies that the consideration of only longitudinal forcing parameters, for example, $\partial_x b$ and U_* in the Simpson number, is not sufficient for a prediction of the stratification.

Strong stratification during ebb suppresses the eddy viscosity and gives rise to strong shear. Thus, the tidal asymmetry of stratification, eddy viscosity, and shear is high and drives an intense longitudinal tidal straining circulation in medium channels. Since this is the dominant contribution to the total residual longitudinal circulation in tidally energetic, weakly (primarily) stratified estuaries, the estuarine circulation is maximum in these medium channels.

In wide channels, 2SIPS and other transverse processes are very weak, that is, hardly any additional stratification is induced, so that the tidal straining circulation is comparably weak. Very wide channels are laterally homogeneous and resemble a one-dimensional situation.

In narrow channels, transverse processes (mainly 2SIPS and vertically, tertiary advected and strain-induced periodic stratification, 3ASIPS) are very strong, and stable stratification is induced already before full flood and persists throughout ebb. 1SIPS further increases the stratification, but this also gives rise to the shear, which eventually produces turbulence and thus decreased stratification and increased eddy viscosity during ebb. This reverse tidal asymmetry of eddy viscosity leads to a reverse tidal straining circulation.

The total, estuarine circulation does not reverse because the advectively driven contribution is the dominant one in narrow channels. As suggested by Lerczak and Geyer (2004), the intensity of the advectively driven circulation increases with the aspect ratio.

Acknowledgments. The studies of Elisabeth Schulz have been funded by a scholarship from the University of Rostock, Interdisciplinary Faculty, Department Maritime Systems. The work of Henk M. Schuttelaars has been supported by a visiting scientist grant through the Leibniz Institute for Baltic Sea Research Warnemünde. Ulf Gräwe has been funded by the German Federal Ministry of Research and Education (BMBF) in the framework of the project PACE (The future of the Wadden Sea sediment fluxes: Still keeping pace with sea level rise?, FKZ 03F0634A). The work of Hans Burchard has been carried out in the framework of the project ECOWS (Role of Estuarine Circulation for Transport of Suspended Particulate Matter in the Wadden Sea) funded by the German Research Foundation (DFG, project BU1199/11). We thank Lars Umlauf (Leibniz Institute for Baltic Sea Research Warnemünde, Rostock, Germany) for valuable discussions and hints. The authors are furthermore grateful to the two anonymous reviewers, whose remarks and suggestions helped to greatly improve this paper.

APPENDIX A

Equations and Reduced Experiments

The hydrostatic dynamic equations along (x, u) and across (y, v) the estuary can be written as follows (assumptions as in section 2a):

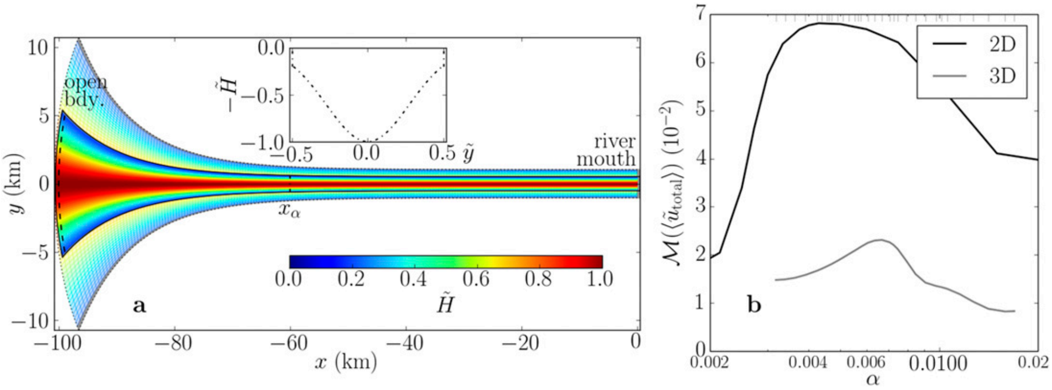

FIG. B1. (a) Topography of the 3D model for $W_{\min} = 1$ km (2 km in lighter shading). (b) Measure of the intensity of the estuarine circulation for varying aspect ratio in the 2D model (total in Fig. 2, for comparison) and in the 3D model at $x_\alpha = -60$ km [see (a)]; the short bars at the upper abscissa mark the $\alpha(x_\alpha)$ values of the individual 3D simulations.

$$\partial_t u + v\partial_y u + w\partial_z u - \partial_z(A_z\partial_z u) - \partial_{y*}(A_{y*}\partial_{y*}u) = \int_z^0 [\partial_x b]\, d\hat{z} - [P_x], \quad \text{and} \tag{A1}$$

$$\partial_t v + v\partial_y v + w\partial_z v - \partial_z(A_z\partial_z v) - \partial_{y*}(A_{y*}\partial_{y*}v) = \int_z^0 \partial_y b\, d\hat{z} - P_y, \tag{A2}$$

where ∂_{y*} is the quasi-horizontal partial derivative along σ layers and P is the barotropic pressure gradient in the given direction. Here, square brackets, [ ], are used to denote prescribed variables.

The budget equation for the salinity is

$$\partial_t S + u[\partial_x S] + v\partial_y S + w\partial_z S - \partial_z(K_z\partial_z S) - \partial_{y*}(K_{y*}\partial_{y*}S) = 0, \tag{A3}$$

where $K_z(y, z, t)$ is the vertical eddy diffusivity.

The reference experiment A (full physics) uses the full Eqs. (A1)–(A3). The reduced experiments (section 3a) are implemented as follows:

experiment C: no momentum advection,
  $v\partial_y u = w\partial_z u = 0$ in (A1) and
  $v\partial_y v = w\partial_z v = 0$ in (A2);
experiment D: no lateral internal pressure gradient, that is, no transverse circulation,
  $\partial_y b = 0$ in (A2); and
experiment F: no transverse salinity advection,
  $v\partial_y S = w\partial_z S = 0$ in (A3).

APPENDIX B

Three-Dimensional Model

Three-dimensional simulations are carried out by means of the General Estuarine Transport Model (GETM). The model domain has a horizontal resolution of 200 × 60 cells and a vertical resolution of 20 sigma layers with zooming toward the bottom.

The topography is shown in Fig. B1a. The initial salinity decreases linearly from S_a at the open boundary, $x = -L$, to 0 at $x = -L/2$ and is 0 between $x = -L/2$ and the river mouth, $x = 0$. The prescribed parameters are listed in Table B1.

TABLE B1. Prescribed parameters for the 3D simulations. The stars mark varied parameters; others are invariant.

	Prescribed parameters		Values/ranges
	L	Length (from river mouth to open boundary)	100 km
★	$W_{\max} = 10W_{\min}$	Maximum width (open boundary)	7.5 – 42.5 km
★	$W_{\min}$	Minimum width (river mouth)	0.75 – 4.25 km
	$H_{\max}$	Maximum water depth (thalweg)	15 m
	$H_{\min}$	Minimum water depth (shoals)	3 m
	η_a	Surface elevation amplitude at open boundary	2 m
	S_a	Salinity at open boundary	32 psu
★	$Q = W_{\min} \times 0.1\,\text{m}^2\,\text{s}^{-1}$	River discharge ($S = 0$ psu)	75 – 425 m^3 s^{-1}
★	$\alpha(x_\alpha) = H_{\max}/W(x_\alpha)$	Aspect ratio at $x_\alpha = -60$ km	0.003 – 0.017

The model is forced by a constant river discharge and an M_2 tidal surface elevation at the open boundary (ω and T as in Table 1),

$$\eta_{\mathrm{bdy}}(t) = \eta_a \sin(\omega t). \qquad \text{(B1)}$$

Simulations are started from rest and run for 20 tidal cycles to ensure periodicity.

The aspect ratio is varied by means of the width (about 30 simulations); the river discharge is scaled accordingly (see Table B1) in order to yield comparable residual velocities. The intensity of the estuarine circulation is analyzed at $x_\alpha = -60\,\mathrm{km}$, which lies at the up-estuary end of the convergence zone.

It should be noted that the convergence increases with the width, but it is very weak at x_α [convergence number $\mathrm{Co} = 2.9 \times 10^{-4}$–$3.2 \times 10^{-4}$; cf. Burchard et al. (2014); that is, increasing by a factor of 1.1 over the covered α range]. Here, the amplitude of the cross-sectionally averaged longitudinal velocity is about $1.3\,\mathrm{m\,s^{-1}}$ and the residual cross-sectionally averaged longitudinal salinity gradient is about $-4 \times 10^{-4}\,\mathrm{psu\,m^{-1}}$. The salinity field exhibits weak primary SIPS (not shown).

The impact of the aspect ratio on the intensity of the estuarine circulation is shown in Fig. B1b. The intensity and thus the absolute impact of the aspect ratio (i.e., the intensity range) are considerably weaker in the three-dimensional model than in the two-dimensional model. This might be related to the spatial and temporal variability of the longitudinal salinity gradient, $\partial_x S(x, y, z, t)$ (constant in the two-dimensional model). However, the qualitative behavior and the relative impact of the aspect ratio are in good agreement.

In the three-dimensional model, the intensity has a maximum at $\alpha \approx 0.0067$. As in the two-dimensional model (also see Fig. 2), this is due to a maximum of the tidal straining circulation, which is again related to secondary SIPS (not shown).

REFERENCES

Agnew, R., 1960: Estuarine currents and tidal streams. *Coastal Eng. Proc.,* **7,** 510–535.

Banas, N. S., and B. M. Hickey, 2005: Mapping exchange and residence time in a model of Willapa Bay, Washington, a branching, macrotidal estuary. *J. Geophys. Res.,* **110,** C11011, doi:10.1029/2005JC002950.

Becherer, J., and L. Umlauf, 2011: Boundary mixing in lakes: 1. Modeling the effect of shear-induced convection. *J. Geophys. Res.,* **116,** C10017, doi:10.1029/2011JC007119.

——, H. Burchard, G. Flöser, V. Mohrholz, and L. Umlauf, 2011: Evidence of tidal straining in well-mixed channel flow from microstructure observations. *Geophys. Res. Lett.,* **38,** L17611, doi:10.1029/2011GL049005.

——, M. T. Stacey, L. Umlauf, and H. Burchard, 2015: Lateral circulation generates flood-tide stratification and estuarine exchange flow in a curved tidal inlet. *J. Phys. Oceanogr.,* **45,** 638–656, doi:10.1175/JPO-D-14-0001.1.

Buckingham, E., 1914: On physically similar systems; Illustrations of the use of dimensional equations. *Phys. Rev.,* **4,** 345–376, doi:10.1103/PhysRev.4.345.

Buijsman, M., and H. Ridderinkhof, 2008: Variability of secondary currents in a weakly stratified tidal inlet with low curvature. *Cont. Shelf Res.,* **28,** 1711–1723, doi:10.1016/j.csr.2008.04.001.

Burchard, H., and R. Hofmeister, 2008: A dynamic equation for the potential energy anomaly for analysing mixing and stratification in estuaries and coastal seas. *Estuarine Coastal Shelf Sci.,* **77,** 679–687, doi:10.1016/j.ecss.2007.10.025.

——, and R. D. Hetland, 2010: Quantifying the contributions of tidal straining and gravitational circulation to residual circulation in periodically stratified tidal estuaries. *J. Phys. Oceanogr.,* **40,** 1243–1262, doi:10.1175/2010JPO4270.1.

——, and H. M. Schuttelaars, 2012: Analysis of tidal straining as driver for estuarine circulation in well-mixed estuaries. *J. Phys. Oceanogr.,* **42,** 261–271, doi:10.1175/JPO-D-11-0110.1.

——, G. Flöser, J. V. Staneva, T. H. Badewien, and R. Riethmüller, 2008: Impact of density gradients on net sediment transport into the Wadden Sea. *J. Phys. Oceanogr.,* **38,** 566–587, doi:10.1175/2007JPO3796.1.

——, F. Janssen, K. Bolding, L. Umlauf, and H. Rennau, 2009: Model simulations of dense bottom currents in the western Baltic Sea. *Cont. Shelf Res.,* **29,** 205–220, doi:10.1016/j.csr.2007.09.010.

——, R. D. Hetland, E. Schulz, and H. M. Schuttelaars, 2011: Drivers of residual estuarine circulation in tidally energetic estuaries: Straight and irrotational channels with parabolic cross section. *J. Phys. Oceanogr.,* **41,** 548–570, doi:10.1175/2010JPO4453.1.

——, H. M. Schuttelaars, and W. R. Geyer, 2013: Residual sediment fluxes in weakly-to-periodically stratified estuaries and tidal inlets. *J. Phys. Oceanogr.,* **43,** 1841–1861, doi:10.1175/JPO-D-12-0231.1.

——, E. Schulz, and H. M. Schuttelaars, 2014: Impact of estuarine convergence on residual circulation in tidally energetic estuaries and inlets. *Geophys. Res. Lett.,* **41,** 913–919, doi:10.1002/2013GL058494.

Chant, R. J., 2002: Secondary circulation in a region of flow curvature: Relationship with tidal forcing and river discharge. *J. Geophys. Res.,* **107,** 3131, doi:10.1029/2001JC001082.

de Boer, G. J., J. D. Pietrzak, and J. C. Winterwerp, 2008: Using the potential energy anomaly equation to investigate tidal straining and advection of stratification in a region of freshwater influence. *Ocean Modell.,* **22,** 1–11, doi:10.1016/j.ocemod.2007.12.003.

Geyer, W. R., 1993: Three-dimensional tidal flow around headlands. *J. Geophys. Res.,* **98,** 955–966, doi:10.1029/92JC02270.

——, and J. D. Smith, 1987: Shear instability in a highly stratified estuary. *J. Phys. Oceanogr.,* **17,** 1668–1679, doi:10.1175/1520-0485(1987)017<1668:SIIAHS>2.0.CO;2.

——, and P. MacCready, 2014: The estuarine circulation. *Annu. Rev. Fluid Mech.,* **46,** 175–197, doi:10.1146/annurev-fluid-010313-141302.

Giddings, S. N., D. A. Fong, and S. G. Monismith, 2011: Role of straining and advection in the intratidal evolution of stratification, vertical mixing, and longitudinal dispersion of a shallow, macrotidal, salt wedge estuary. *J. Geophys. Res.,* **116,** C03003, doi:10.1029/2010JC006482.

——, and Coauthors, 2012: Frontogenesis and frontal progression of a trapping-generated estuarine convergence front and its influence on mixing and stratification. *Estuaries Coasts,* **35,** 665–681, doi:10.1007/s12237-011-9453-z.

Hansen, D. V., and M. Rattray Jr., 1965: Gravitational circulation in straits and estuaries. *J. Mar. Res.,* **23,** 104–122.

Howlett, E. R., T. P. Rippeth, and J. Howarth, 2011: Processes contributing to the evolution and destruction of stratification in the Liverpool Bay ROFI. *Ocean Dyn.,* **61,** 1403–1419, doi:10.1007/s10236-011-0402-y.

Huijts, K. M., H. E. de Swart, G. P. Schramkowski, and H. M. Schuttelaars, 2011: Transverse structure of tidal and residual flow and sediment concentration in estuaries. *Ocean Dyn.,* **61,** 1067–1091, doi:10.1007/s10236-011-0414-7.

Ianniello, J. P., 1979: Tidally induced residual currents in estuaries of variable breadth and depth. *J. Phys. Oceanogr.,* **9,** 962–974, doi:10.1175/1520-0485(1979)009<0962:TIRCIE>2.0.CO;2.

Jay, D. A., and J. D. Musiak, 1994: Particle trapping in estuarine tidal flows. *J. Geophys. Res.,* **99,** 20 445–20 461, doi:10.1029/94JC00971.

——, and ——, 1996: Internal tidal asymmetry in channel flows: origins and consequences. *Mixing in Estuaries and Coastal Seas,* C. Pattiaratchi, Ed., Coastal and Estuarine Studies, Vol. 50, Amer. Geophys. Union, 211–249.

Kalagnanam, J., M. Henrion, and E. Subrahmanian, 1994: The scope of dimensional analysis in qualitative reasoning. *Comput. Intell.,* **10,** 117–133, doi:10.1111/j.1467-8640.1994.tb00160.x.

Kundu, P. K., and I. M. Cohen, 2002: *Fluid Mechanics.* 2nd ed. Academic Press, 730 pp.

Lacy, J. R., M. T. Stacey, J. R. Burau, and S. G. Monismith, 2003: Interaction of lateral baroclinic forcing and turbulence in an estuary. *J. Geophys. Res.,* **108,** 3089, doi:10.1029/2002JC001392.

Lerczak, J. A., and W. R. Geyer, 2004: Modeling the lateral circulation in straight, stratified estuaries. *J. Phys. Oceanogr.,* **34,** 1410–1428, doi:10.1175/1520-0485(2004)034<1410:MTLCIS>2.0.CO;2.

Linden, P. F., 1979: Mixing in stratified fluids. *Geophys. Astrophys. Fluid Dyn.,* **13,** 3–23, doi:10.1080/03091927908243758.

——, 1980: Mixing across a density interface produced by grid turbulence. *J. Fluid Mech.,* **100,** 691–703, doi:10.1017/S002211208000136X.

——, and J. E. Simpson, 1986: Gravity-driven flows in a turbulent fluid. *J. Fluid Mech.,* **172,** 481–497, doi:10.1017/S0022112086001829.

——, and ——, 1988: Modulated mixing and frontogenesis in shallow seas and estuaries. *Cont. Shelf Res.,* **8,** 1107–1127, doi:10.1016/0278-4343(88)90015-5.

MacCready, P., and W. R. Geyer, 2010: Advances in estuarine physics. *Annu. Rev. Mar. Sci.,* **2,** 35–58, doi:10.1146/annurev-marine-120308-081015.

Nunes, R. A., and J. H. Simpson, 1985: Axial convergence in a well-mixed estuary. *Estuarine Coastal Shelf Sci.,* **20,** 637–649, doi:10.1016/0272-7714(85)90112-X.

Peters, H., 1997: Observations of stratified turbulent mixing in an estuary: Neap-to-spring variations during high river flow. *Estuarine Coastal Shelf Sci.,* **45,** 69–88, doi:10.1006/ecss.1996.0180.

Pritchard, D. W., 1952: Salinity distribution and circulation in the Chesapeake Bay estuarine system. *J. Mar. Res.,* **11,** 106–123.

Purkiani, K., J. Becherer, G. Flöser, U. Gräwe, V. Mohrholz, H. M. Schuttelaars, and H. Burchard, 2015: Numerical analysis of stratification and destratification processes in a tidally energetic inlet with an ebb tidal delta. *J. Geophys. Res. Oceans,* **120,** 225–243, doi:10.1002/2014JC010325.

Scully, M. E., and C. T. Friedrichs, 2007: The importance of tidal and lateral asymmetries in stratification to residual circulation in partially mixed estuaries. *J. Phys. Oceanogr.,* **37,** 1496–1511, doi:10.1175/JPO3071.1.

——, and W. R. Geyer, 2012: The role of advection, straining, and mixing on the tidal variability of estuarine stratification. *J. Phys. Oceanogr.,* **42,** 855–868, doi:10.1175/JPO-D-10-05010.1.

——, C. Friedrichs, and J. Brubaker, 2005: Control of estuarine stratification and mixing by wind-induced straining of the estuarine density field. *Estuaries,* **28,** 321–326, doi:10.1007/BF02693915.

——, W. R. Geyer, and J. A. Lerczak, 2009: The influence of lateral advection on the residual estuarine circulation: A numerical modeling study of the Hudson River estuary. *J. Phys. Oceanogr.,* **39,** 107–124, doi:10.1175/2008JPO3952.1.

Simpson, J. H., D. J. Crisp, and C. Hearn, 1981: The shelf-sea fronts: Implications of their existence and behaviour. *Philos. Trans. Roy. Soc. London,* **A302,** 531–546, doi:10.1098/rsta.1981.0181.

——, J. Brown, J. Matthews, and G. Allen, 1990: Tidal straining, density currents, and stirring in the control of estuarine stratification. *Estuaries,* **13,** 125–132, doi:10.2307/1351581.

Smith, R., 1976: Longitudinal dispersion of a buoyant contaminant in a shallow channel. *J. Fluid Mech.,* **78,** 677–688, doi:10.1017/S0022112076002681.

Souza, A. J., 2013: On the use of the Stokes number to explain frictional tidal dynamics and water column structure in shelf seas. *Ocean Sci.,* **9,** 391–398, doi:10.5194/os-9-391-2013.

Stacey, M. T., S. G. Monismith, and J. R. Burau, 1999: Observations of turbulence in a partially stratified estuary. *J. Phys. Oceanogr.,* **29,** 1950–1970, doi:10.1175/1520-0485(1999)029<1950:OOTIAP>2.0.CO;2.

——, J. R. Burau, and S. G. Monismith, 2001: Creation of residual flows in a partially stratified estuary. *J. Geophys. Res.,* **106,** 17 013–17 037, doi:10.1029/2000JC000576.

Valle-Levinson, A., 2008: Density-driven exchange flow in terms of the Kelvin and Ekman numbers. *J. Geophys. Res.,* **113,** C04001, doi:10.1029/2007JC004144.

——, C. Li, K.-C. Wong, and K. M. M. Lwiza, 2000: Convergence of lateral flow along a coastal plain estuary. *J. Geophys. Res.,* **105,** 17 045–17 061, doi:10.1029/2000JC900025.

van Rijn, L. C., 2011: Analytical and numerical analysis of tides and salinities in estuaries; Part I: Tidal wave propagation in convergent estuaries. *Ocean Dyn.,* **61,** 1719–1741, doi:10.1007/s10236-011-0453-0.

Waterhouse, A. F., and A. Valle-Levinson, 2010: Transverse structure of subtidal flow in a weakly stratified subtropical tidal inlet. *Cont. Shelf Res.,* **30,** 281–292, doi:10.1016/j.csr.2009.11.008.

——, B. Tutak, A. Valle-Levinson, and Y. P. Sheng, 2013: Influence of two tropical storms on the residual flow in a subtropical tidal inlet. *Estuaries Coasts,* **36,** 1037–1053, doi:10.1007/s12237-013-9606-3.

Winant, C. D., 2008: Three-dimensional residual tidal circulation in an elongated, rotating basin. *J. Phys. Oceanogr.,* **38,** 1278–1295, doi:10.1175/2007JPO3819.1.